Journal of Marine Research, 65, 27–58, 2007

Mean jets, mesoscale variability and eddy momentum fluxes in the surface layer of the Antarctic Circumpolar Current in Drake Passage

by Y.-D. Lenn[1,2], T. K. Chereskin[1], J. Sprintall[1], and E. Firing[3]

ABSTRACT

High-resolution Acoustic Doppler Current Profiler (ADCP) observations of surface-layer velocities in Drake Passage, comprising 128 sections over a period of 5 years, are used to study the surface-layer circulation of the Antarctic Circumpolar Current (ACC). These observations resolve details of the mean flow including the topographic control of the mean Subantarctic Front (SAF) and the multiple filaments of the Polar Front (PF) and Southern ACC Front (SACCF) that converge into single mean jets as the ACC flows through Drake Passage. Subsurface definitions of the SAF and PF applied to expendable bathythermograph temperatures generally coincide with mean jets, while the SACCF is better defined in velocity than temperature. The mean transport in the top 250-m-deep surface layer, estimated from the cross-track transport along three repeat tracks, is 27.8 ± 1 Sv.

Eddy momentum fluxes were estimated by ensemble averaging Reynolds stresses relative to gridded Eulerian mean currents. Eddy kinetic energy (EKE) is surface intensified in the mixed layer because of inertial currents and decreases poleward in Drake Passage, ranging from $\sim 800\,\mathrm{cm^2\,s^{-2}}$ to $\sim 200\,\mathrm{cm^2\,s^{-2}}$. ADCP EKE estimates are everywhere significantly higher than altimetric EKE estimates, although the pattern of poleward decrease is the same. Horizontal-wavenumber spectra of velocity fluctuations peak at wavelengths in the 250–330 km range and are significantly anisotropic. Along-passage fluctuations dominate at wavelengths less than 250 km; cross-passage fluctuations dominate at wavelengths greater than 250 km. Mesoscale eddies dominate the variance in northern Drake Passage. Inertial variability is constant with latitude and together with baroclinic tides accounts for some but not all of the discrepancy between the ADCP surface-layer EKE and altimetry-inferred EKE.

1. Introduction

The Antarctic Circumpolar Current (ACC) flows through the South Pacific, Atlantic and Indian oceans, driven by strong zonal winds unimpeded by continents. This makes the ACC a uniquely important conduit for heat, salt and freshwater exchange between all the world's

1. Scripps Institution of Oceanography, University of California, La Jolla, California, 92093, U.S.A.
2. Corresponding author: ***email: ylenn@ucsd.edu***
3. Department of Oceanography, School of Ocean and Earth Science and Technology, University of Hawaii at Manoa, Honolulu, HI 96822, U.S.A.

major oceans. Despite the importance of the ACC, high-resolution long-term observations have been limited by the remoteness and inhospitable nature of the Southern Ocean.

The landmark International Southern Ocean Studies (ISOS) experiment employed a series of hydrographic cruises and year-long mooring deployments of current meters and pressure gauges, during the period 1975–1980, to measure the flow in Drake Passage (Nowlin *et al.*, 1977; Pillsbury *et al.*, 1979; Sciremammano *et al.*, 1980; Whitworth and Peterson, 1985). These observations showed that in Drake Passage, the ACC flow is concentrated in three narrow vertically-coherent bands of strong eastward velocity that separate 4 distinct water masses (Nowlin *et al.*, 1977). These three jets were associated with the steepening of the poleward-shoaling isopycnals and are now commonly referred to as the Subantarctic Front (SAF), the Polar Front (PF) and the Southern ACC Front (SACCF) (Nowlin *et al.*, 1977; Emery, 1977; Whitworth, 1980; Orsi *et al.*, 1995, (hereafter referred to as O95) and Figure 1). Annual mean net transport above 2500 m was established to be 124.7 ± 9.9 Sv (Whitworth and Peterson, 1985) and 9.1 ± 5.3 Sv below 2500 m (Whitworth, 1983).

Renewed long-term observations in Drake Passage began in 1993, with annual occupations of a hydrographic and lowered Acoustic Doppler Current Profiler section (SR1), from Burdwood Bank to Elephant Island in austral summer (Fig. 1). Cunningham *et al.* (2003) estimated the transport relative to the deepest common level between adjacent station pairs to be 136.7 ± 7.8 Sv from six SR1 hydrographic sections and included the ISOS data in an analysis of the ACC variability. Cunningham *et al.* (2003) observed the SAF and PF to be highly variable, meandering on interannual timescales. The interannual frontal variability was corroborated by Sprintall (2003) from repeat high-resolution expendable bathythermograph (XBT) surveys in Drake Passage.

These results have deepened our understanding of the ACC and its variability. However, the ISOS and the SR1 sections cover different time periods and locations in Drake Passage and are therefore insufficient for resolving the filaments and branching of the ACC flow suggested by numerical models (e.g. Maltrud *et al.*, 1998; Hughes and Ash, 2001). Various climatologies (Olbers *et al.*, 1992; Levitus and Boyer, 1994; Gouretski and Jancke, 1998) estimate the mean Southern Ocean flow, but at low resolutions dictated by the sparse historical hydrography. Estimates of Southern Ocean dynamic height from neutrally buoyant floats (Gille, 2003a) and surface drifters (Niiler *et al.*, 2003) have significant unresolved differences that may be due in part to Stokes drift or the wind-slip of the drifter drogues, effects that must be measured directly. Furthermore, high eddy kinetic energies seen in the ACC by satellite altimeters (Morrow *et al.*, 1994; Stammer, 1998) have yet to be verified by measurements of currents and estimates of eddy momentum fluxes in the mixed layer. This is because moorings tend to be deployed well below the mixed layer to limit mooring motion from current drag and escape damage by icebergs.

A new set of underway observations in Drake Passage presents an exciting opportunity to quantify the mean surface-layer currents and the associated eddy momentum fluxes. Since September 1999, surface-layer currents have been measured with a ship-mounted Acoustic Doppler Current Profiler (ADCP) from the U. S. Antarctic Program vessel, the R/V *Laurence*

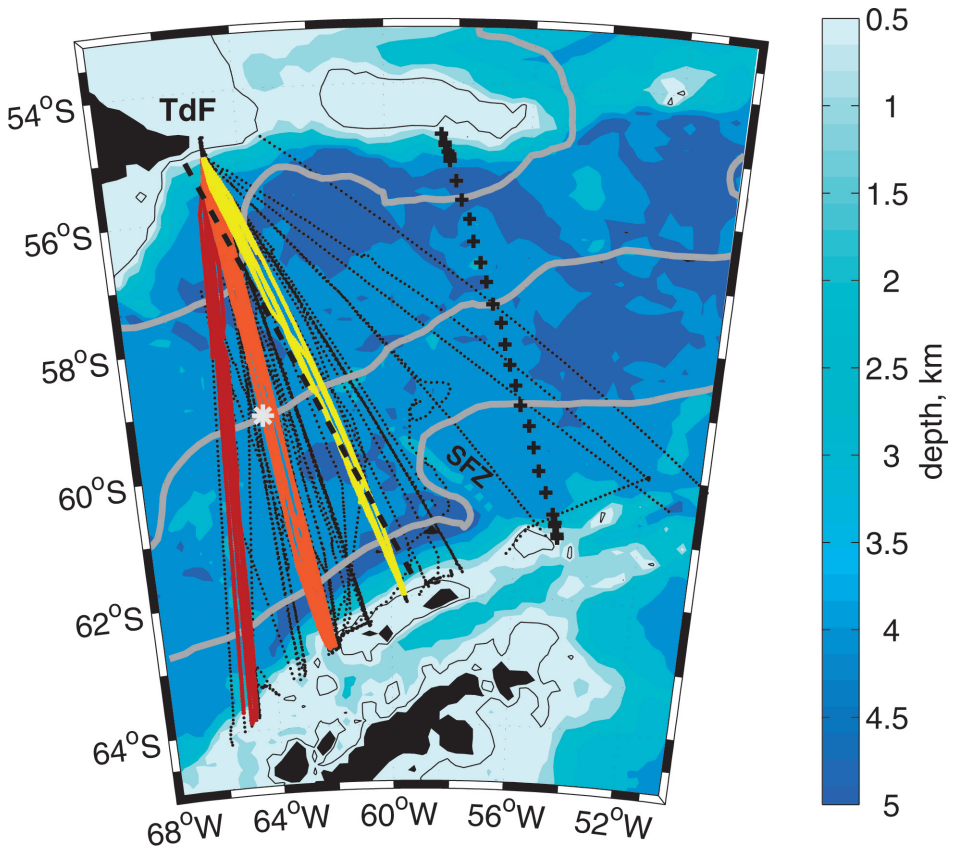

Figure 1. Map of Drake Passage showing bathymetry (bluescale) together with the 200-m depth contour (thin black). Also plotted are the mean SAF, PF and SACCF from Orsi *et al.* (1995) (thick grey lines), hydrographic stations of the SR1 line (Cunningham *et al.*, 2003) (crosses), the location of the ISOS/FDRAKE mooring (light asterisk), the y-axis of the down/cross passage coordinate system (dashed line) and LMG cruise tracks in Drake Passage from September 1999 to December 2004 (dotted black lines). Full and partial transects associated with the **W**est (30), **M**iddle (56) and **E**ast (26) repeat tracks are shown (red, orange and yellow). Tierra del Fuego (TdF) marks the common northern end of the LMG Drake Passage crossings, and the Shackleton Fracture Zone is labelled (SFZ).

M Gould (LMG) (Chereskin *et al.*, 2000). The LMG is the principal supply ship for Palmer Station, Antarctica and crosses Drake Passage twice monthly on average, allowing for an ADCP data set unprecedented in both temporal and spatial resolution ($\leq$5 km along-track). This study employs the LMG ADCP data to define the mean jets and mesoscale currents at high resolution and to estimate surface-layer transport in Drake Passage (Section 3). In Section 4, eddy momentum fluxes and eddy kinetic energies, as represented by the Reynolds stresses of velocity, are computed to characterize surface layer mesoscale variability. Length

scales of variability are examined using Fourier wavenumber spectral analysis. The inertial component of the surface-layer mesoscale variability is estimated from the ADCP observations and validated by moored observations and currents simulated from reanalysis winds. Moored observations also provide an estimate of the contribution to variability from baroclinic tides. Results are discussed in Section 5, and conclusions are presented in Section 6.

2. Instrumentation and data

a. High-resolution ADCP observing program

The ADCP data used in this analysis were collected aboard the LMG during supply trips to Palmer Station and scientific cruises around the Antarctic Peninsula and the Scotia Sea. This analysis uses ADCP data from 128 Drake Passage crossings from September 1999 to December 2004. The LMG cruise tracks span Drake Passage, spreading south, east and west from Tierra del Fuego (TdF, Fig. 1) and are concentrated in the western half of the region. Three oft-repeated tracks occupied by the LMG lie in the west (W), middle (M) and east (E) of the highly-sampled region. In this study, observations that lie within 25-km-wide swaths centered on the exactly repeating tracks are grouped together (Fig. 1). Though irregular in time and space, the LMG data set provides a time series of highly-resolved surface-layer currents in Drake Passage and continues to be augmented as part of an ongoing observation program (Chereskin *et al.*, 2000).

Ocean currents are sampled by a 153.6 kHz RD Instruments ADCP mounted in the hull of the LMG. The transducer is installed in a sonar pod that deflects the ice and bubble-laden boundary layer, so the velocity profiles consistently extend to 300 m. The ADCP is configured with nominal 8-m bin and 16-m pulse lengths; the shallowest bin is centered at 26 m. Pings are averaged in 300-s ensembles. Gyrocompass headings are corrected with an Ashtech GPS attitude sensing array (King and Cooper, 1993), and the ship-relative currents are referenced to earth using P-code GPS. Since March 2003, civilian GPS has been used as its accuracy is comparable to P-code GPS now that it is no longer subject to dithering by the Department of Defense ("Selective Availability"). The speed of sound through antifreeze, in which the transducer is immersed, is measured by a sensor in the transducer well and used to calculate the ADCP velocity scale factor. Data are processed and edited using the CODAS3 software (http://currents.soest.hawaii.edu/software/codas3).

The deep water barotropic tide predicted by the TPXO6.2 model (Egbert *et al.*, 1994) is removed from all the ADCP velocities presented. Measurement errors in the absolute velocities computed from 15-min ensemble averages are 1 cm s^{-1} (Chereskin and Harding, 1993; Chereskin and Harris, 1997) and are considerably less than the standard deviation of currents in Drake Passage, which are ~30–60 cm s^{-1} over the record length of the observations in any given location.

In Drake Passage the mean flow is not strictly zonal and is more naturally represented in Cartesian co-ordinates that roughly parallel the continental boundaries. For this study we have chosen down/cross passage Cartesian co-ordinates (x_{pc}, y_{pc}) that are rotated 23.6°

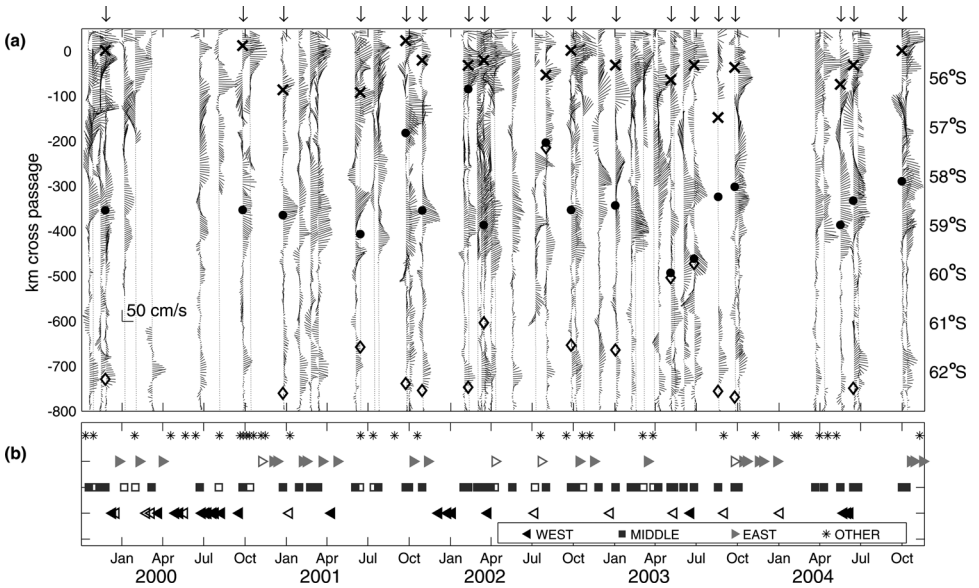

Figure 2. (a) Stick plots of detided ADCP currents at 150-m depth along the repeat track M (Fig. 1) observed between September 1999 and December 2004. Current vectors are shown projected in passage Cartesian co-ordinates such that the down-passage velocity component is parallel to the time-axis, and the cross-passage velocity component is parallel to the y-axis; corresponding latitudes are shown along the right y-axis. Times of XBT surveys are indicated by the arrows along the top; XBT-inferred positions of the SAF, PF and SACCF are marked as ($\times$, $\bullet$, $\diamond$) respectively. Temporal distribution of the Drake Passage crossings are shown in (b): crossings are sorted into West (black triangles), Middle (dark grey squares), East (light grey triangles) repeat transects and other non-repeat transects (black asterisks). Transects that complete more than 90% of the repeat crossings are indicted by filled symbols and partially-occupied repeat transects are indicted by open symbols.

anti-clockwise from north such that the $x_{pc} = 0$ line coincides with the dashed line in Figure 1. ADCP currents are shown projected into this co-ordinate system unless specified otherwise.

Mean surface-layer velocities along the three repeat tracks are computed from full and partial Drake Passage transects coincident with each repeat track: 30 for track W, 56 for track M and 26 for track E. The temporal distribution of Drake Passage crossings coinciding with full and partial occupations of the three repeat tracks and other non-repeat tracks is shown in Figure 2b. The partial sections generally coincide with the northern halves of each repeat line. Calculation of cross-track transport for each repeat line is limited to full repeat transects and includes 19 transects along track W, 21 transects along track M and 18 transects along track E. For the transport calculation, missing data in the 26-m to 250-m depth range is linearly interpolated and extrapolated in the vertical from existing data in the relevant velocity profile.

Standard errors throughout this study were calculated by dividing the standard deviations by the square root of the number of degrees of freedom. Bryden (1979) found that velocities observed at deep moored current meters in Drake Passage became decorrelated after 10–12 days on average. The average temporal separation between the end of one Drake Passage crossing and the start of the next crossing is 12 days, and the average temporal separation between crossings of the middle of Drake Passage, where the PF is located, is 15 days. Therefore we assume that each Drake Passage transect accounts for one degree of freedom.

b. High-resolution XBT observations

The high-resolution repeat XBT surveys of Drake Passage were also conducted by the LMG and are ongoing (Sprintall, 2003). This study encompasses 37 XBT surveys coincident with the ADCP velocities between September 1999 and December 2004. Details of the repeat XBT observations are described by Sprintall (2003). XBT probes are deployed every 6–10 km across the SAF and PF and every 10–15 km elsewhere between the 200-m isobaths at either end of Drake Passage. The XBT probes consistently return water temperatures down to 800 m. These XBT surveys are conducted approximately 6 times per year; thus the post-September 1999 XBT surveys coincide with roughly 30% of the ADCP sections. There were 7 XBT surveys along track W, 17 surveys along track M and 6 surveys along track E.

c. AVISO altimetry

The CLS-Space Oceanography Division produces a merged altimetric product of weekly sea-level anomalies. The AVISO (DT-REF) product combines altimetric observations from Topex/Poseidon, ERS, GFO, JASON and Envisat to produce objectively-mapped sea-level anomalies on a 1/3° Mercator grid (Le Traon *et al.*, 1997; Ducet *et al.*, 2000). Sea-level anomalies from October 1994 to December 2004 were used in this study.

d. LMG ADCP and ECMWF reanalysis winds

On the LMG, ocean winds are measured with two R. M. Young anemometers mounted at 30 m above the reference waterline on the port and starboard sides of the ship. The measurements are recorded every $2\frac{1}{2}$ minutes from both anemometers. The starboard anemometer was the default sensor for computing true wind speed, but the port sensor was used when the starboard sensor was downwind of the ship's superstructure. All anemometer observations from the LMG are corrected to 10 m above sea level using the Large and Pond (1981) bulk formulas for open ocean wind measurements.

The European Center for Medium-range Weather Forecasts produces a reanalysis wind product, ERA-40. This product assimilates data from multiple satellites measuring numerous atmospheric and ocean parameters as well as ship and terrestrial observations in a global reanalysis (Uppala *et al.*, 2005). The ERA-40 data is available for the period from September 1957 to August 2002; this study employs the 10-meter wind fields at 6 hour $\times$ 2.5° latitude $\times$ 2.5° longitude resolution for the period September 1999 to August 2002.

In a comparison of two reanalysis wind products with station observations at high and mid latitudes in the Southern Hemisphere, Bromwich and Fogt (2004) found that skill in the ERA-40 winds is generally higher than the other widely-used reanalysis product from the National Centers for Environmental Prediction-National Center for Atmospheric Research. This is particularly true after the inception of satellite observations in 1978, as the ERA-40 reanalysis is more strongly constrained by the satellite observations which are often the only observations of winds over the open ocean.

3. Drake Passage surface-layer currents

Jets and high mesoscale and temporal variability characterize the surface-layer currents in Drake Passage. This is clearly seen in a time series of horizontal currents at 150-m depth, from 56 full or partial transects, along the most often repeated M track (Fig. 2a). The surface-layer flow is predominantly down-passage, with relatively quiescent flow in the $-600\,\mathrm{km} \leq y_{pc} \leq -450\,\mathrm{km}$ range separating larger currents of $\sim$40–50 cm s^{-1} on most transects. Reversals in the flow are common and are often associated with large eddying features. At the southern end, where $y_{pc} = -700\,\mathrm{km}$, there is a persistent narrow jet of $\sim 40\,\mathrm{cm\,s^{-1}}$ flowing down-passage located at the approximate position of the SACCF. A bigger jet with typical amplitudes $\geq 50\,\mathrm{cm\,s^{-1}}$, located at the very northern end of the transect is another constant feature and is associated with the SAF. Both these frontal jets vary in amplitude, direction and width from transect to transect. In between the SAF and SACCF, multiple jets and flow reversals produced by the mesoscale variability make it difficult to conclusively identify the instantaneous PF frontal jet. The mesoscale activity can have similar length scales and amplitudes as the frontal jets.

Numerous definitions exist for determining the ACC front positions from upper ocean temperatures (O95, Botnikov, 1963; Joyce *et al.*, 1978; Sokolov and Rintoul, 2002; Belkin and Gordon, 1996). The SAF is located by the maximum subsurface temperature gradient between the 4°C and 5°C isotherms at 400-m depth (O95, Sprintall, 2003). The northernmost extent of the 2°C isotherm at a depth of 200 m defines the PF (O95, Botnikov, 1963; Joyce *et al.*, 1978; Sprintall, 2003), and the SACCF is located at the intersection of the 1.8°C isotherm with the depth of the maximum temperature gradient (O95). The XBT-inferred SAF and PF front locations generally coincide with surface velocity jets (Fig. 2a). In contrast, the XBT-inferred position of the SACCF varies widely across passage and does not always coincide with the small jet at $y_{pc} = -700$ km seen in most of the synoptic sections.

a. Mean fronts and jets

The ADCP and XBT observations along each full and partially-occupied repeat section are averaged together to estimate the mean currents, eddy kinetic energy $\left(\mathrm{EKE} = \frac{1}{2}\left(\overline{u'^2_{pc}} + \overline{v'^2_{pc}}\right)\right)$ and shear variance $\left(\overline{\left(\frac{du}{dz}\right)^2} + \overline{\left(\frac{dv}{dz}\right)^2}\right)$ in Drake Passage (Fig. 3 and 4). In the standard error calculation (Fig. 3e), the number of degrees of freedom at each latitude is equal to the number of transects coincident with each repeat track up to a maximum of 30 for the West

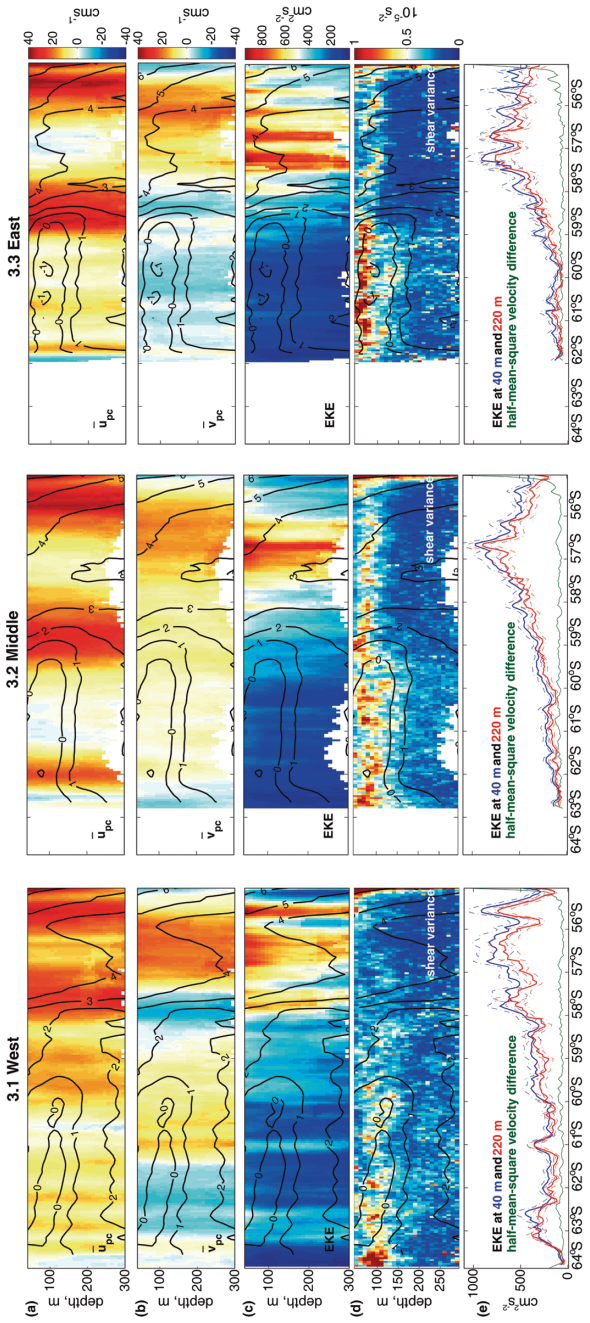
3.1 West
3.2 Middle
3.3 East
(a)
(b)
(c)
(d)
(e)
depth, m
cm s-1
cm2 s-2
10-5 s-2
EKE
shear variance
EKE at 40 m and 220 m
half-mean-square velocity difference
64°S 63°S 62°S 61°S 60°S 59°S 58°S 57°S 56°S

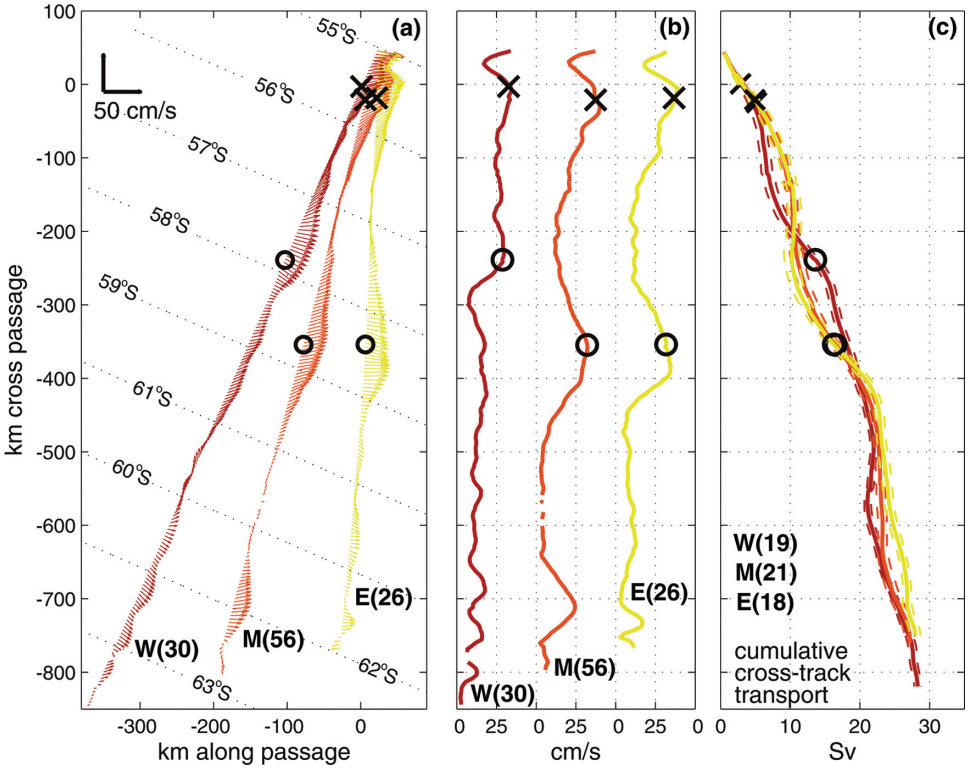

Figure 4. Mean currents observed along the repeat tracks W (red), M (orange), E (yellow) shown as (a) stick plots of statistically significant detided depth-averaged horizontal currents, (b) magnitudes of the total depth-averaged velocity and (c) cumulative cross-track transport between the Drake Passage 500-m isobaths, projected back into passage co-ordinates. The locations of the SAF(×) and PF (o), inferred from the mean XBT temperature sections are also shown. The number of transects that contribute to each calculation are shown in parentheses.

track (Fig. 3.1), 56 for the Middle track (Fig. 3.2) and 26 for the East track (Fig. 3.3). All the mean values are shown in the vertical sections (Fig. 3) while the few mean currents that are not statistically significant are omitted from Figure 4a and 4b. The majority of the estimated mean currents are statistically significant, and the standard errors exceed the estimate of mean currents (Fig. 4a and 4b) only where the mean currents are very small (Fig. 3).

Figure 3. Mean vertical sections for the (3.1) **W**est (3.2) **M**iddle and (3.3) **E**ast repeat tracks (Fig. 1). The panels in each subfigure are (a) detided mean down-passage velocity, (b) detided mean cross-passage velocity, (c) eddy kinetic energy (EKE), (d) mean shear variance and (e) EKE values at 40 m (blue) and 220 m (red) and the corresponding half-mean-square velocity difference (green); the dashed lines mark the range of the standard errors. Mean values at depths where there are fewer than 15 repeat observations are not shown. Mean temperature contours from the respective repeat XBT surveys are superposed (thick black lines).

The mean Drake Passage flow is more ordered than in the synoptic sections, with vertically coherent, strong down-passage currents separated by much weaker mean currents (Figs. 3.1, 3.2, 3.3 and 4). A distinct jet is present in all three vertical sections of mean down-passage velocities at locations where the 5°C isotherm is steepest and associated with the SAF. The mean XBT temperatures along track W, computed from 7 surveys spanning all 4 seasons, indicate the presence of an eddy just south of the SAF (Fig. 3.1a). The eddy is also present in mean velocity calculated from the same 7 ADCP transects (not shown) but is not present in the mean calculated from 30 full and partial W transects (Fig. 3.1a) or in a 6-year mean temperature section (not shown).

The PF jet on track W appears to have two filaments with the stronger branch coincident with the northern extent of the 2°C isotherm and a weaker branch coincident with the northern extent of the 1°C isotherm (Fig. 3.1a, 4a and 4b). This is because the synoptic 2°C isotherm at 200 m in the 7 XBT W-sections is found at one of two latitudes: the mean 2°C isotherm is representative of the northerly latitude (∼57.9 S), and the mean 1°C isotherm is representative of the southerly latitude (∼59.5 S, Fig. 3.1a). In the mean velocity section, the two PF branches appear to coalesce downstream, as the mean M and E sections show the 1°C and 2°C isotherms converging in location and coinciding with a jet similar in amplitude to the combined upstream branches of the PF (Fig. 4a and 4b). Similarly, three narrow jets at the southern end of track W (Fig. 3.1a) appear downstream in tracks M and E as a single well-defined jet (Fig. 3.2a, 3.3a and 4a). Across-passage variations in mean-velocity magnitudes show that the jet widths of the PF and SAF, as defined by the lateral separation of the half-peak velocity magnitudes in each mean frontal jet, are 150 km and 75 km respectively in Drake Passage (Fig. 4b). The instantaneous SAF and PF frontal jets can be seen to vary laterally in position and their widths range from 50 km to 150 km in the time-series of currents along track M (Fig. 2a). The meandering of these fronts broadens the time-average width of each frontal jet.

The Drake Passage current variance is represented by the EKE. High EKE between the 2°C and 5°C isotherms indicates that the variability is concentrated between the SAF and PF in Drake Passage (Fig. 3c). EKE at 40-m and 220-m depths, above and below the mean mixed layer respectively, indicates that the peak values of EKE between the fronts of $\sim 900\,\mathrm{cm^2\,s^{-2}}$ are significantly higher than the average EKE values of about $200\,\mathrm{cm^2\,s^{-2}}$ found south of the PF along tracks M and E (Fig. 3.2e and 3.3e). The decrease in EKE values south of the PF is less dramatic on track W. Differences in EKE at 40-m and 220-m depths very rarely exceed the standard errors, but the energy at 40-m depth is always slightly higher.

A subsurface maximum in shear variance, higher in the southern half of Drake Passage, is present in all three vertical sections (Fig. 3d). There is good agreement between the shear variance maximum and the depth and equatorward extent of the sub-surface temperature minimum on track W. On tracks M and E the shear maximum extends northwards of the temperature minimum (Fig. 3d). Away from the shear maximum, the shear variance is small ($\sim 2 \times 10^{-6}\,\mathrm{s^{-1}}$) in the surface layer along all three tracks. The half-mean-square

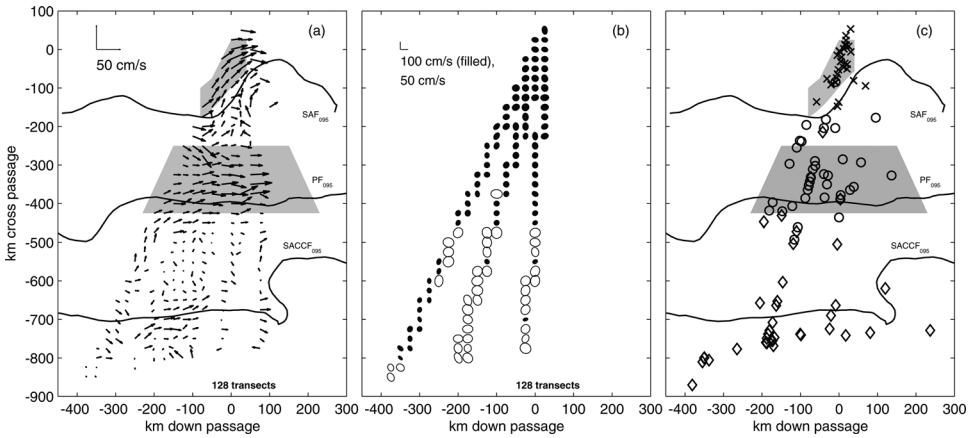

Figure 5. (a) Depth-averaged, detided, gridded mean of surface-layer currents (30–300 m) shown where grid boxes are crossed thrice or more. (b) Standard deviation ellipses of the depth-averaged ADCP currents; ellipses with major axes greater than 37 cm s^{-1} are filled. Grid boxes crossed less than 15 times are omitted; scale vectors, 100 (filled) and 50 (unfilled) cm s^{-1}, are shown. (c) Positions of the SAF (x), PF(o) and SACCF (diamond) inferred from subsurface XBT temperatures during the LMG observation period. Mean positions of the SAF, PF and SACCF from O95 are plotted as thick solid lines in (a) and (c) and labeled SAF_{O95}, PF_{O95} and $SACCF_{O95}$. The grey background shading in (a) and (c) highlight the mean SAF and PF jets.

velocity difference between 40-m and 220-m depths is ∼60–70 cm^2 s^{-2} and independent of latitude, except at the very northern end of the sections where the shear variance is also high (Fig. 3.1e, 3.2e and 3.3e).

Using all the LMG ADCP observations we defined Eulerian-mean currents on a 25 km × 25 km grid, by first averaging the ADCP velocities by transect and then averaging over all the transects (time) and depths in each grid box (Fig. 5a). This Eulerian mean resolves the flow between the 3 repeat tracks, providing a more complete view of the surface-layer circulation in Drake Passage (Fig. 5). Gray background shading highlights currents associated with the mean SAF and PF (Fig. 5a and 5c). The small jet seen at the southern end of repeat tracks M and E (Fig. 4a) flows into Drake Passage from the west and veers northwards as it travels along passage (Fig. 5). The jet is co-located with the mean SACCF determined by O95 from historical hydrography and is north of most of the instantaneous SACCF positions inferred from XBT temperatures (Fig. 5c). The XBT-inferred SACCF positions vary meridionally more than the other XBT-inferred front positions.

The mean PF appears as a broad jet flowing down passage through the concentration of XBT-inferred PF front positions (Fig. 5a and 5c), with a core located 50 km north of the mean O95 PF. The two branches of the PF seen on track W (Fig. 4a) appear in the larger pattern as a convergence of flow entering Drake Passage from the northwest and southwest (Fig. 5a) and become more aligned down passage.

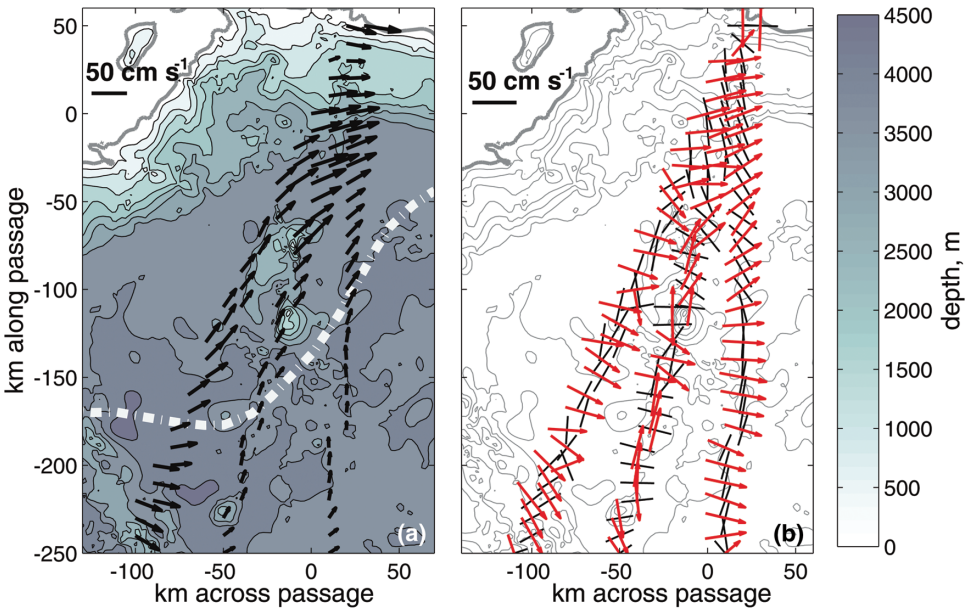

Figure 6. (a) Finely-gridded mean surface-layer currents that differ significantly from zero and (b) corresponding major (red) and minor (black) axes of the standard deviation ellipses are shown for each 10 km ×10 km grid box crossed more than 15 times north of the mean PF in Drake Passage. Bathymetry ((a) grayscale; (b) thin gray contours at 500-m intervals) and the 200 m isobath (gray line) are also shown. The SAF determined by Orsi *et al.* (1995) (white dashed dotted line) is located approximately at the southern edge of the mean SAF jet.

Of the three ACC frontal jets, the location of the observed SAF mean jet agrees best with the closely clustered XBT-inferred front positions (Fig. 5a and 5c). Unlike the mean SACCF and PF jets that are directed mainly down-passage, the SAF jet veers sharply northwards as it enters Drake Passage from the west. Statistically significant mean currents along the repeat tracks in northern Drake Passage, gridded at higher resolution in 10 km × 10 km grid boxes, show the SAF jet following the bathymetry of the Patagonian continental slope more closely than the mean O95 SAF position (Fig. 6a). The position of the mean O95 SAF loosely corresponds with the southern edge of the mean gridded SAF jet.

Velocity variance in the Eulerian-mean currents is represented by the standard deviation ellipses in Figure 5b. These ellipses are plotted with a dual scale such that the filled ellipses are twice as energetic as the open ellipses. This scale highlights the striking pattern of higher velocity variance in the PF and northwards in the Drake Passage study region. The velocity variance south of the PF along track W is higher than the variances downstream and associated with the multiple small jets (Fig. 3.1a and 4a). The major axes of the standard deviation ellipses for the finely-gridded currents (Fig. 6a) are aligned with the direction of the mean current (Fig. 6b) in the region close to the Patagonian continental slope and along

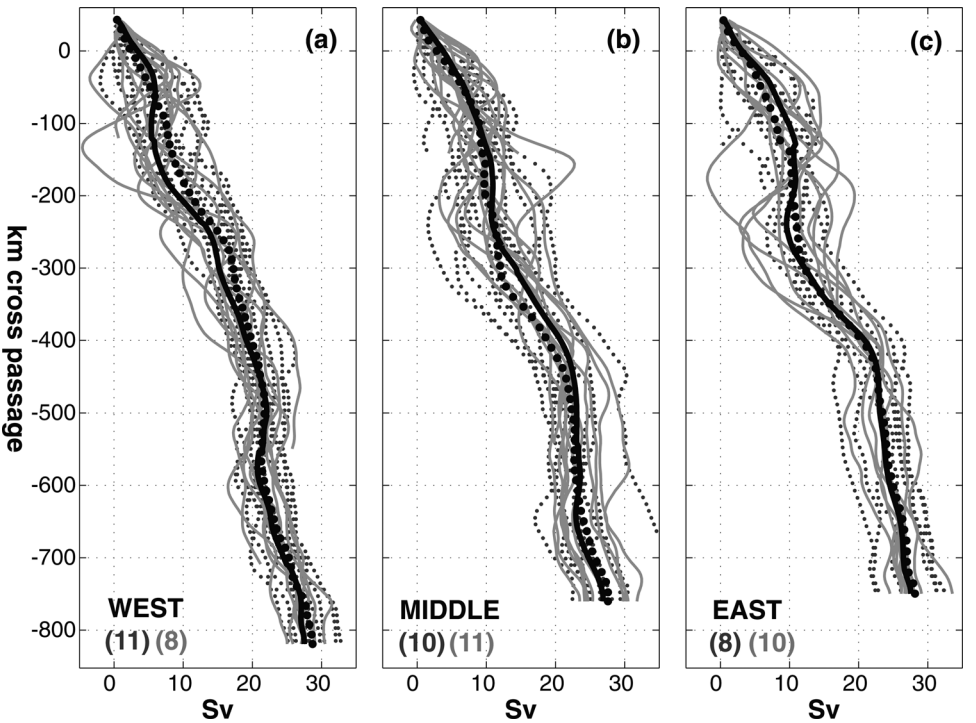

Figure 7. Cumulative transport in the top 250 m in Drake Passage, between the 500 m isobaths of the Patagonian and Antarctic continental slopes, calculated from the ADCP observations along the (a) West, (b) Middle and (c) East repeat tracks. The number of southbound transects (light grey lines) and northbound transects (dark grey dotted lines) is shown in each panel. Mean cumulative transports for the southbound (thick black lines) and northbound transects (thick black dotted lines) for each repeat line are superposed. Note that the cumulative transport calculations include only full and partial repeat sections that are continuous at the northern end of the transect.

track M. However, the standard deviation ellipses south of the SAF along tracks W and E are not aligned with the mean currents.

b. Cumulative surface-layer transports

Cumulative cross-track surface-layer transports provide another view of Drake Passage flow patterns. The cumulative cross-track transports in the top 250 m were calculated for each of the three repeat transects beginning at the 500-m isobath of the Patagonian continental slope and ending at the 500-m isobath of the Antarctic continental slope (Fig. 7). Repeat tracks W, M and E cross the Patagonian slope 500-m isobath within 2 km of each other. The top 26-m layer is assumed to move as a slab with the 26-m-bin velocity. As noted in Section 2a, partial transects were excluded from this calculation such that only 19 W transects, 21 M transects and 18 E transects were utilized. Data gaps were filled by linear

interpolation and extrapolation in the vertical of the relevant velocity profile. Southbound and northbound crossings are evenly distributed along each repeat track and indicate that the cumulative surface transports are not biased by LMG heading (Fig. 7) or season. The cross-track transports are plotted against the projection of along-track distance onto the y_{pc} axis (Fig. 4c and 7).

The synoptic cumulative transports increase poleward, with numerous along-track oscillations due to inertial and mesoscale variability, and punctuated by several large increases in transport at the frontal jets (Fig. 7). On all three repeat lines, steep gradients at $-100\,\text{km} \leq y_{pc} \leq 50\,\text{km}$ correspond to the SAF, and on tracks M and E, steep gradients at $-400\,\text{km} \leq y_{pc} \leq -300\,\text{km}$ correspond to the PF. The fluctuations are large north of $y_{pc} = -450\,\text{km}$, particularly on track E.

Averaging the synoptic cumulative transports reduces the along-track mesoscale variability and emphasizes the contribution of the mean frontal jets to the surface-layer transport (Fig. 4c). Steep increases in the mean cumulative surface transports coincide with velocity maxima and the mean XBT-inferred SAF and PF positions along the three tracks (Fig. 4b and 4c). Along tracks M and E, the PF is associated with an increase of ~10 Sv between $y_{pc} = -450$ km and $y_{pc} = -250$ km (Fig. 4c). A similar transport increase occurs over a longer section (-500 km $\leq y_{pc} \leq -200$ km) of track W (Fig. 4c), reflecting the more filamented structure of the PF as it enters Drake Passage (Fig. 4a). Though weakest of the ACC fronts, the mean SACCF frontal jet is present along all three tracks (Fig. 4a and b), but steep gradients in mean cumulative transport at -650 km $\leq y_{pc} \leq -700$ km are seen on only tracks W and M (Fig. 7b and 4c).

The total mean W, M and E surface-layer transports are 28.3 ± 1 Sv, 27.2 ± 1 Sv and 27.9 ± 1 Sv (Fig. 4c). Standard errors were calculated assuming 19 degrees of freedom for track W, 21 for track M and 18 for track E. The surface-layer transports of the three repeat lines do not differ significantly at the 95% confidence level, represented by ± 4 Sv error bars. Therefore the mean surface-layer transport in Drake Passage is 27.8 ± 1 Sv, computed by averaging the three mean repeat estimates, each weighted by the number of transects. Our calculations indicate that the top 250 m accounts for 20% of the total 136.7 ± 7.8 Sv of ACC transport in Drake Passage reported by Cunningham *et al.* (2003).

Transport anomalies, calculated relative to respective total surface transports of each repeat transect, confirm that the variability in total surface transport is substantial and can be ~10 Sv on timescales shorter than a month (Fig. 8). Insufficient complete transects along each repeat line prohibit the resolution of the seasonal signal. No significant trend in the total surface-layer transport is observed during our observation period.

4. Variability in the surface-layer currents

Eddy momentum fluxes, as represented by Reynolds stresses, were estimated from the ADCP observations to better quantify the Drake Passage surface-layer variability. Velocity anomalies are calculated as described for the 25×25 km gridded currents (Section 3a)

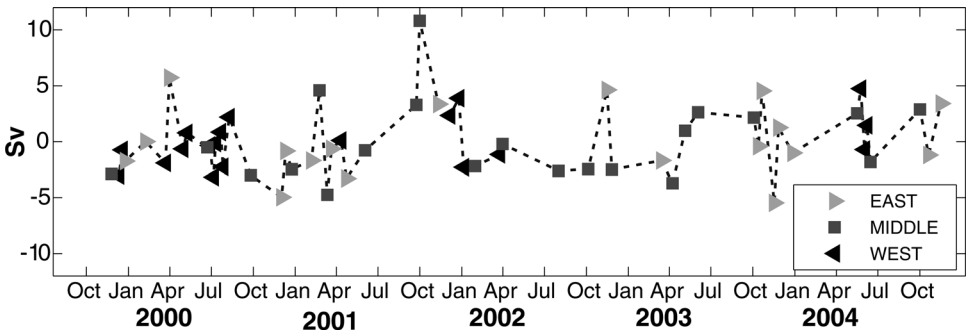

Figure 8. Time series of surface-layer transport anomalies, relative to the respective mean surface-layer transports, are shown for West (black triangles), Middle (dark grey boxes) and East (light grey triangles) repeat tracks.

by subtracting the mean surface-layer currents (Fig. 5a). The Reynolds stresses, $\langle\overline{u'u'}\rangle$, $\langle\overline{v'v'}\rangle$, $\langle\overline{u'v'}\rangle$ and EKE are then ensemble-averaged over all the estimates in each grid box and finally averaged by depth. Note that all the eddy momentum fluxes are presented as momentum fluxes per unit density; a typical density for the surface layer in Drake Passage is 1027 kg m^{-3} (Levitus and Boyer, 1994). The broader spatial sampling of the gridded estimates (Fig 5b and 9a) fills in the pattern seen in the repeat sections (Fig. 3c).

Averaged by regions delineated by the alternating gray and white background shading shown in Figure 5, momentum fluxes north of the PF are at least twice as high as those south of the PF (Table 1). North of the PF, a marked anisotropy is present in the velocity variances such that $\langle\overline{u'u'}\rangle$ is significantly higher than $\langle\overline{v'v'}\rangle$ in the SAF while the opposite is true in the region between the SAF and PF. Across Drake Passage the momentum flux $\langle\overline{u'v'}\rangle$ is negative and significant between the fronts but does not differ significantly from zero elsewhere. EKE between the SAF and PF is more than 4 times the EKE south of the PF. Finally, momentum fluxes and EKE calculated for the top 120 m are higher than the estimates in the lower layer (120-m to 300-m depth). These differences are significant at 95% confidence (twice the standard errors) except in the region between the SAF and PF (Table 1).

An independent estimate of EKE was calculated from 10-years of weekly AVISO sea-level anomalies such that

$$EKE_{sla} = \frac{1}{2}\left(u'^2_{sla} + v'^2_{sla}\right) = \frac{1}{2}\left(\frac{g}{f}\right)^2 \left\langle \frac{\partial(SLA)}{\partial x}^2 + \frac{\partial(SLA)}{\partial y}^2 \right\rangle \quad (1)$$

where g is gravitational acceleration, SLA is the sea-level anomaly. The distribution of the altimetric EKE matches the ADCP EKE distribution in Drake Passage, with the highest values between the SAF and PF (Fig. 9). However, the altimetric EKE estimates are markedly lower than the ADCP EKE estimates, with a difference of $\sim$300 cm^2 s^{-2} in northern Drake Passage (Table 3).

Table 1. Average surface-layer eddy momentum fluxes per unit density ($cm^2\ s^{-2}$) in Drake Passage. Velocities are rotated into down/cross-passage co-ordinates as described in Section 2a. Eddy fluxes are averaged over separate regions within Drake Passage to reflect the spatial distribution of eddy momentum. Standard errors are shown for $\langle\overline{u'u'}\rangle$, $\langle\overline{v'v'}\rangle$ and $\langle\overline{u'v'}\rangle$; the 95% confidence limit corresponds to two standard errors.

	Observed (ADCP) Momentum Fluxes ($cm^2\ s^{-2}$):			
Region	$\langle\overline{u'u'}\rangle$	$\langle\overline{v'v'}\rangle$	$\langle\overline{u'v'}\rangle$	EKE
SAF	681 ± 35	500 ± 37	-8 ± 23	591 ± 25
Between Fronts	647 ± 62	923 ± 96	-75 ± 45	785 ± 57
PF	367 ± 26	371 ± 26	-11 ± 15	369 ± 19
South of PF	164 ± 9	183 ± 12	2 ± 6	174 ± 7
		upper layer : 30 m to 120 m		
SAF	753 ± 33	538 ± 37	-6 ± 25	645 ± 25
Between Fronts	678 ± 60	969 ± 95	-94 ± 42	824 ± 56
PF	400 ± 28	399 ± 29	-11 ± 15	400 ± 20
South of PF	184 ± 9	202 ± 13	0.1 ± 6	193 ± 8
		lower layer : 120 m to 300 m		
SAF	627 ± 31	472 ± 36	-9 ± 22	550 ± 24
Between Fronts	624 ± 62	889 ± 97	-60 ± 47	756 ± 58
PF	341 ± 24	349 ± 24	-11 ± 14	345 ± 17
South of PF	150 ± 8	169 ± 11	4 ± 6	159 ± 7

a. Resolving horizontal length scales

The horizontal-wavenumber spectra of along- and cross-passage velocities at each depth were computed from ADCP observations interpolated to 5-km intervals along-track. Variance-preserving spectra were calculated by averaging these spectra over all 128 transects and over all depths; variations in depth were slight (not shown). Band averaging is performed at wavenumbers greater than 0.01 cycles per km ($\lambda < 100$ km). The 90% confidence limits were estimated using a χ^2-distribution where the minimum number of degrees of freedom was 128. The along-passage velocity spectrum peaks at 0.004 cycles per km (250 km wavelength) with spectral power falling off rapidly with increasing wavenumber (Fig 10a). A peak occurs at 0.003 cycles per km (330 km wavelength) in the cross-passage velocity spectrum, with a similar decrease in spectral power with increasing wavenumber. The two spectral peaks are broad and overlap by more than the resolution bandwidth (0.001 cycles per km) of the wavenumber spectra. Therefore the peak wavenumbers of the down- and cross-passage velocity spectra are not distinguishable from each other. The mean ACC frontal jets flow mainly along passage and would thus contribute variance primarily to the along-passage velocity spectra; anisotropy between the two spectra is significant at wavenumbers greater than 0.004 cycles per km (Fig. 10a).

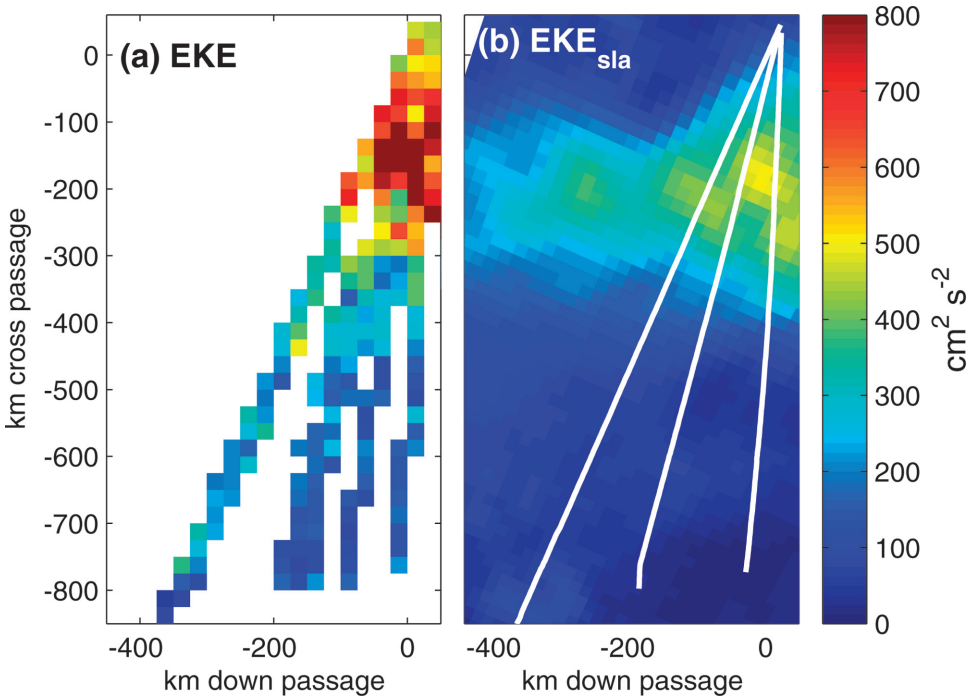

Figure 9. Maps of eddy kinetic energy, EKE ($cm^2\ s^{-2}$), computed (a) from ADCP velocities referenced to the gridded mean currents and averaged from 30-m to 300-m depth, (b) from objectively mapped sea-level anomalies of the Topex/Poseidon and ERS-merged altimetric product. Typical errors are given in Table 1, grid boxes crossed fewer than 15 times are omitted in (a) and white lines mark the location of repeat tracks W, M and E in (b).

The contribution of the mean ACC frontal jets is excluded by re-computing the spectra from the ADCP-velocity anomalies (Fig. 10b), calculated relative to the gridded mean currents (Fig. 5a). There is a decrease in the peak variance from about $260\,cm^2\ s^{-2}$ to $200\,cm^2\ s^{-2}$ in the along-passage ADCP-anomalies spectra. Not surprisingly, the cross-passage velocity spectrum is changed only slightly when the mean is removed (Fig. 10a and 10b). The location of the ADCP-anomalies spectral peaks, and the anisotropy of the down- and cross-passage anomalies spectra at wavenumbers greater than 0.004 cycles per km are similar to the total velocity spectra because they are dominated by the anomalies. Variance at wavelengths greater than 100 km represents 85% of the total variance of the combined down- and cross-passage velocity spectra.

Horizontal-wavenumber spectra were also computed for geostrophic surface velocity anomalies, inferred from the AVISO sea-level anomalies, and interpolated to the locations and times of the LMG ADCP observations (Fig. 10b). The spectral peaks in the geostrophic anomalies occur at one resolution bandwidth lower than their ADCP anomaly counterparts (Fig. 10b), but the spectral peak bandwidths overlap. Both components of the geostrophic

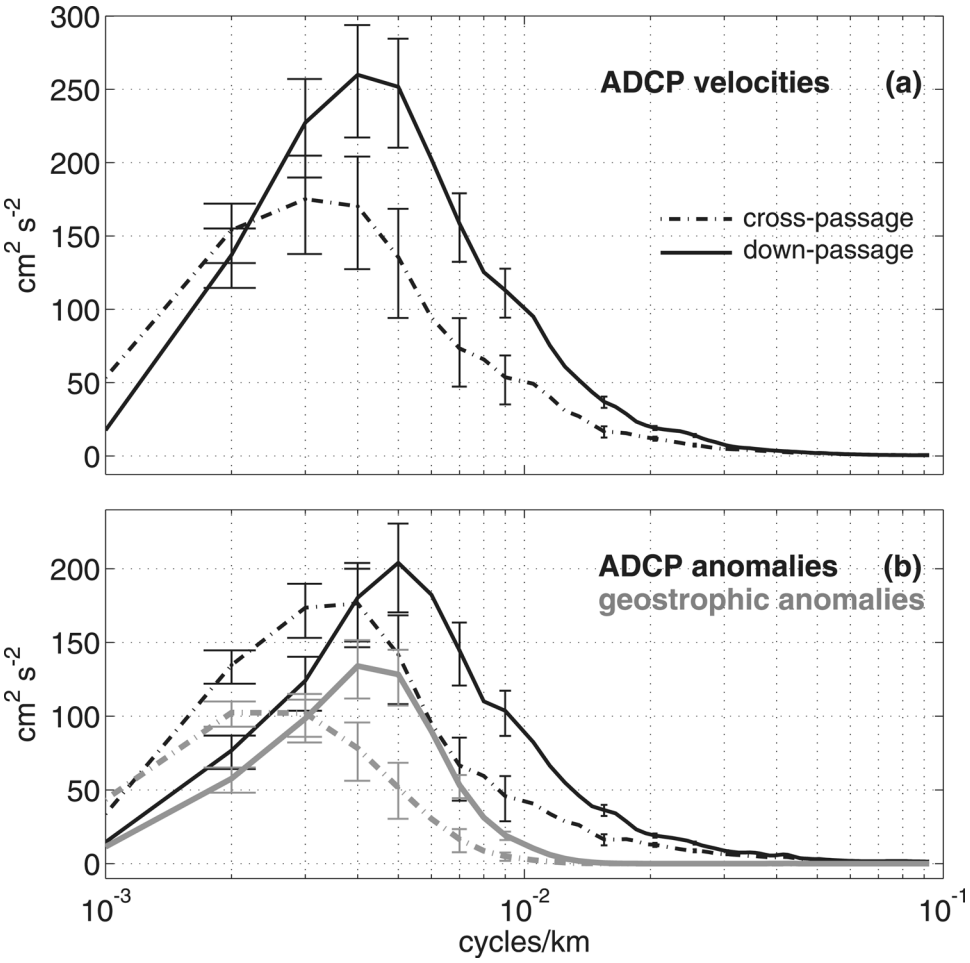

Figure 10. Variance-preserving horizontal-wavenumber spectra, averaged by depth, computed for the (a) total down-passage (black solid lines) and cross-passage velocities (black dashed lines) and (b) down-passage and cross-passage velocity anomalies relative to the gridded-Eulerian-mean currents from 128 ADCP transects. Corresponding spectra for gesotrophic surface velocity anomalies (grey solid and dashed lines), interpolated onto the LMG Drake Passage crossings, are plotted in (b). The sample interval is 5 km along-track distance. Errorbars denote the 90% χ^2 confidence intervals.

anomalies spectra contain significantly less total variance than the ADCP anomalies spectra at all wavelengths. At wavelengths greater than 100 km, the geostrophic anomalies have 56% of the variance in the ADCP velocity anomalies, but only 3% at wavelengths of 100 km or less. In particular, the altimetry underestimates variability with length scales corresponding to the first internal Rossby radius, which decreases poleward from 25 km to 9 km in Drake Passage. To produce the AVISO sea level anomalies, the altimetry data at latitudes above

50S are first subject to a low-pass filter with a 70 km cut-off wavelength and then merged by objective mapping where the spatial decorrelation lengthscale assumed at Drake Passage latitudes is about 100 km (Ducet *et al.*, 2000).

b. Variability from inertial currents

Drake Passage is a notoriously windy place. A probability density function shows that wind speeds of 10 to 15 m s^{-1} are frequently observed by the LMG shipboard anemometer (Fig. 11a). These winds force inertial currents that are not detected by the altimeter, but nonetheless contribute to the variability of the surface-layer currents. Assuming that inertial currents are much weaker and randomly phased below the mixed layer, ADCP velocity differences across the base of the mixed layer ($|\Delta\vec{U}_{ml}|$) provide a proxy for observed inertial

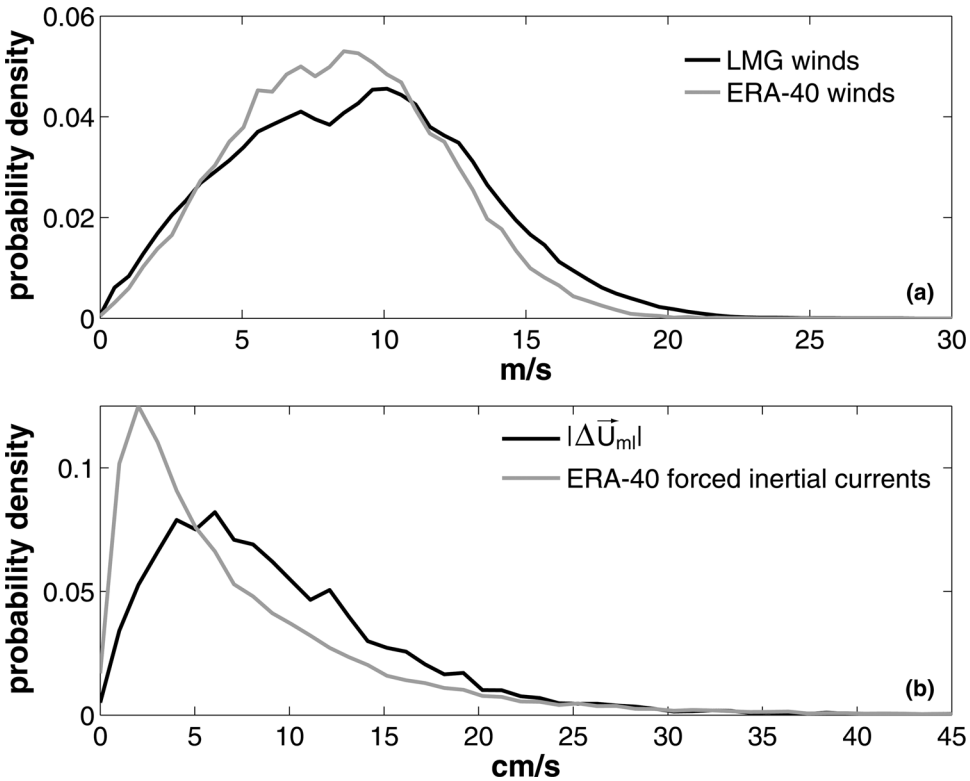

Figure 11. Probability density functions of wind speeds for Drake Passage, as measured by (a) the anemometer on the LMG between August 2000 and June 2004 (black line); (b) the ERA-40 reanalysis winds for the period September 1999 to August 2002 (grey line). The probability density function of inertial currents forced by the ERA-40 winds (grey) and the track W and M across mixed-layer ADCP velocity differences $\frac{1}{2}|\Delta\vec{U}_{ml}|^2$ (black) for the same period are shown in (b).

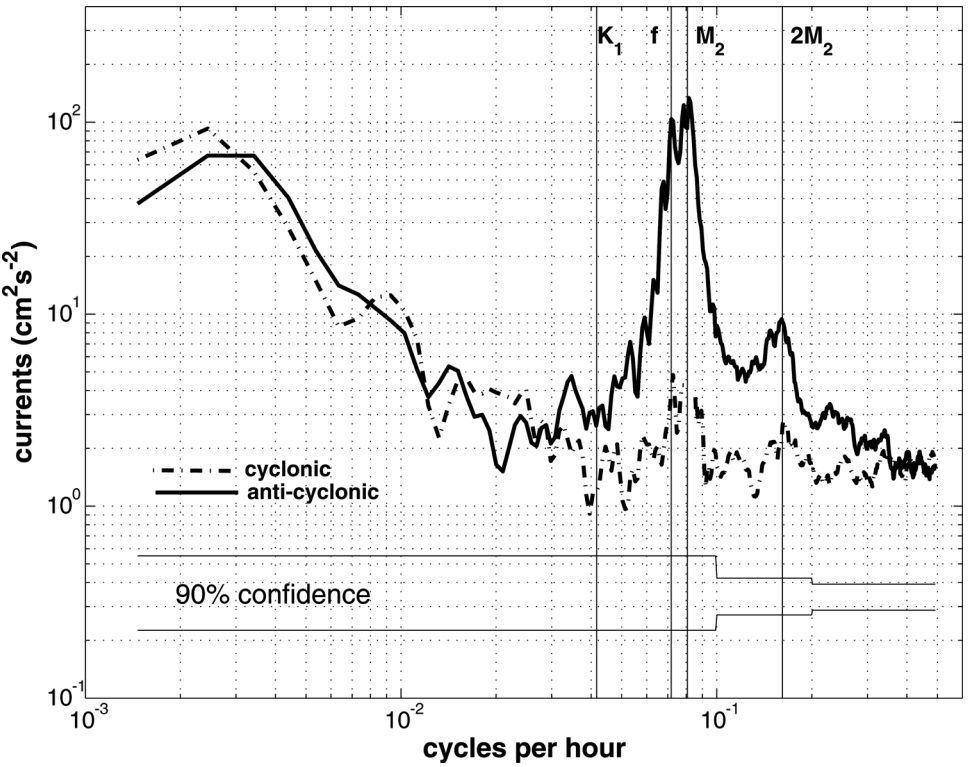

Figure 12. Variance-preserving rotary spectra for currents observed at 235-m depth, from a mooring deployed at 59° S 6.3′ 63° W 49.5′ in Drake Passage, from February to December 1977. Anti-cyclonic (solid line) and cyclonic (dash-dot line) currents, with the barotropic tide predicted by TPXO6.2 removed, are plotted as solid and dashed lines respectively. The frequencies associated with the K_1 diurnal tide, f inertial frequency. M_2 semi-diurnal tide and the first-harmonic, $2M_2$ are shown. The 90% χ^2 confidence interval is shown at the base of the figure.

currents. The inertial current proxy $|\Delta\vec{U}_{ml}|$ was calculated from the velocity differences over a 100-m depth interval centered at the seasonally-varying depth of the shear variance maximum that corresponds to the mixed-layer depth inferred from the XBT temperatures (not shown). The probability density distribution of $|\Delta\vec{U}_{ml}|$ peaks at about 6 cm s^{-1} and is asymmetric with a long tail at speeds greater that 15 cm s^{-1} (Fig. 11b). Inertial contributions to variability inferred from regionally-averaged values of $\frac{1}{2}|\Delta\vec{U}_{ml}|^2$ are 52 ± 15 cm^2 s^{-2} in the SAF, 55 ± 16 cm^2 s^{-2} between the SAF and PF, 61 ± 15 cm^2 s^{-2} in the PF and 67 ± 14 cm^2 s^{-2} south of the PF.

To test the assumption that inertial currents are weak below the mixed layer, inertial current variance below the mixed layer was estimated from variance-preserving rotary spectra computed from the Drake Passage ISOS/FDRAKE moored observations (Fig. 12). The spectra shown here were calculated from the shallowest current meter observations (235-m

depth) located at 59°S 6.3′, 63°W 49.5′ from February to December 1977. These moored observations were well below the mean mixed layer depth in Drake Passage that shoals polewards in Drake Passage from 135 m to 105 m. Spectra calculated from this mooring near the mean PF core (Fig. 1) were characteristic of ISOS/FDRAKE moored observations elsewhere in Drake Passage (not shown). Barotropic tides predicted by the TPXO6.2 model have been subtracted from the moored observations. A peak in the anticyclonic spectra at the inertial frequency indicates the presence of inertial and near-inertial currents and underscores the resonant response of the ocean to wind at the inertial frequency (Fig. 12).

Kinetic energy at near-inertial frequencies below the mixed layer were estimated, as in Alford and Whitmont (2007), by integrating the anticyclonic spectra over the half-peak-power frequency band ($-0.069 \leq \omega \leq -0.076$ cph) centered on the inertial frequency (Fig. 12) and dividing by a factor of two. At 235 m, the near-inertial kinetic energy is $2.4 \leq 3.5 \leq 5.7\,\mathrm{cm^2\,s^{-2}}$ and consistent with $\mathrm{O}(10^{-4}\,\mathrm{J\,kg^{-1}})$ estimates of near-inertial kinetic energy made by Alford and Whitmont (2007) from the same set of historical moorings. The near-inertial kinetic energy from the mooring is considerably less than typical values for $\frac{1}{2}|\Delta\vec{U}_{ml}|^2$ that are $\sim 60\,\mathrm{cm^2\,s^{-2}}$ in Drake Passage. This supports the assumption that inertial currents are mainly contained within the mixed layer.

Aliasing inherent in the irregularly sampled LMG observations of inertial current variability was examined by simulating inertial currents in the region enclosing tracks W and M using the Pollard and Millard (1970) inertial slab model:

$$\left(\frac{\partial}{\partial t} + if + r\right)(u_{in} + iv_{in}) = \frac{F + iG}{H}, \tag{2}$$

where $u_{in} + iv_{in}$ is the complex inertial vector current, f is the Coriolis parameter, r is a decay constant, H is mixed layer depth and $F + iG$ is the vector wind stress. Eqn. 2 was solved in the spectral domain, following the method of Alford (2003), by applying a transfer function to the Fourier transform of the wind forcing that depends on a frequency-dependent decay constant $r(\omega) = 0.15f[1 - e^{-2\omega^2/f^2}]$ and is inversely proportional to H. H was set to the annual mean mixed layer depth. The wind stress was derived from the ECMWF ERA-40 6-hour reanalysis 10-m winds, $\overrightarrow{U_{era}}$, using drag coefficients from Yelland and Taylor (1996). The ERA-40 winds were used as the inertial model requires a continuous time-series of wind forcing at each location, which the LMG shipboard winds do not provide.

The ERA-40 wind speeds in the region enclosing tracks W and M from September 1999 to August 2002 have a similar probability density distribution to the LMG winds observed during the same period, but are skewed to lower wind speeds (Fig. 11a). Inertial currents predicted using the ERA-40 winds in Drake Passage are also skewed to smaller speeds than the observed $|\Delta\vec{U}_{ml}|$ and have an asymmetric probability density distribution that peaks at 2 cm $\mathrm{s^{-1}}$ with a long tail at higher current speeds (Fig. 11b).

Inertial momentum fluxes were computed from the variances and co-variances of: (1) the inertial currents predicted at the times when repeat tracks W and M were occupied (LMG

Table 2. Average inertial current momentum fluxes per unit density ($cm^2\ s^{-2}$) in Drake Passage predicted by forcing the Pollard and Millard (1970) inertial model with the ERA-40 10 meter winds. Velocities are rotated into down/cross-passage co-ordinates as described in Section 2a. Fluxes computed for separate regions within Drake Passage for comparison with the spatial distribution of eddy momentum. Standard errors are shown.

	Predicted Inertial Momentum Fluxes ($cm^2\ s^{-2}$):			
Region	$\langle\overline{u'u'}\rangle$	$\langle\overline{v'v'}\rangle$	$\langle\overline{u'v'}\rangle$	EKE
		LMG sampling		
SAF	27 ± 9	24 ± 7	1 ± 5	25 ± 6
Between Fronts	46 ± 19	49 ± 13	1 ± 9	47 ± 11
PF	41 ± 19	43 ± 13	0.5 ± 9	42 ± 12
South of PF	60 ± 29	58 ± 23	8 ± 16	59 ± 18
		Record Length		
SAF	38 ± 6	33 ± 6	3 ± 3	35 ± 4
Between Fronts	63 ± 10	66 ± 11	4 ± 6	64 ± 7
PF	55 ± 9	54 ± 9	3 ± 5	54 ± 6
South of PF	73 ± 14	62 ± 13	11 ± 9	68 ± 10

Sampling) and (2) the full time series of inertial currents generated by the ERA-40 winds (Record Length) (Table 2). Standard errors are shown for both estimates, such that in case (1) each occupation of W or M tracks is independent and in case (2) every 4-day period, corresponding to approximately 8 inertial periods is considered independent. Within the uncertainties the two sampling schemes give the same results. In both cases the inertial $\langle\overline{u'u'}\rangle$, $\langle\overline{v'v'}\rangle$ and EKE are slightly higher south of the PF than elsewhere, similar to the observed $\frac{1}{2}|\Delta\vec{U}_{ml}|^2$ and in contrast with the higher ADCP-derived EKE values in northern Drake Passage. As expected the inertial variance is isotropic; $\langle\overline{u'v'}\rangle$ is indistinguishable from zero everywhere.

The slab model (Eq. 2), with realistic wind forcing, simulates inertial current variability that is similar in size and latitudinal distribution to the observational proxy for inertial variability $\frac{1}{2}|\Delta\vec{U}_{ml}|^2$. The slab model results also show that temporal aliasing is not significant. Rotary spectra of moored currents below the mixed layer in Drake Passage (Fig. 12) confirm that the inertial currents are generally confined to the mixed layer. These results provide confidence that $\frac{1}{2}|\Delta\vec{U}_{ml}|^2$ is a realistic estimate of the near-inertial EKE in our observations.

c. Variability from baroclinic tides

Baroclinic tides are another source of variability present in the LMG observations. Numerical model predictions of the baroclinic M_2 tidal energy flux vary widely in Drake Passage. Padman *et al.* (2006) report a modest flux of $\sim$160 W m^{-1} along the South Scotia Ridge, a value <1% of the very high fluxes estimated by Simmons *et al.* (2004) for Drake Passage.

The large disparity reflects the difference between a high-resolution regional model with realistic stratification (Padman *et al.*, 2006) and a lower-resolution global model with mid-latitude stratification (Simmons *et al.*, 2004).

There is a peak in spectral power at the M_2 tidal frequency in the Drake Passage currents observed at 235-m depth from the ISOS/FDRAKE mooring (Fig. 12). As the barotropic tides have been excluded, the kinetic energy contained at the M_2 and the first-harmonic $2M_2$ tidal frequencies comes from the M_2 baroclinic tide (Fig. 12). The total kinetic energy in the M_2 peak, $4.0 \leq 5.9 \leq 9.8\,\mathrm{cm^2\ s^{-2}}$ (90% confidence), is close to the inertial-peak kinetic energy and suggests a baroclinic-M_2 amplitude of at most $\sim 3\,\mathrm{cm\,s^{-1}}$. If the $2M_2$ peak is included, the combined baroclinic-tidal kinetic energy is $7.2 \leq 10.1 \leq 15.0\,\mathrm{cm^2\ s^{-2}}$. The internal tides are expected to be dominated by the first-mode baroclinic tide (not shown) which varies little in amplitude over the top 300 m, unlike the inertial currents that are sheared across the base of the mixed layer. The upper-300-m baroclinic tide shear increases as bottom depth decreases on the continental slopes.

5. Discussion

a. Mean flow

Multiple branches of the PF and SACCF entering from the Pacfic Ocean converge, becoming well-defined mean jets in Drake Passage (Figs. 3, 4 and 5), the narrowest choke point of the Southern Ocean. In particular two branches of the PF, observed in the mean W section of velocity and temperature, merge and become a single frontal jet downstream in the M and E sections that eventually flows into the South Atlantic (Figs. 3.1, 3.2 and 3.3). The filamented, branching structure of the ACC fronts has been observed at other locations in the Southern Ocean (Sparrow *et al.*, 1996; Holliday and Read, 1998; Moore *et al.*, 1999; Sokolov and Rintoul, 2002).

Finely-gridded mean currents show the mean SAF clearly following the bathymetric contours of the Patagonian slope (Fig. 6a). The mean PF is well defined although the synoptic PF meanders more widely than the SAF over the smoother bathymetry away from the continental slope. This suggests that topographic control is weaker for the PF than the SAF in Drake Passage, although Drake Passage is one of several locations in the ACC where topographic control of the PF is important (Moore *et al.*, 1999; Sokolov and Rintoul, 2002; Cunningham *et al.*, 2003; Gille, 2003a; Dong *et al.*, 2006). The mean SACCF and indeed the synoptic SACCF, as seen along track M, are in good agreement with the O95 SACCF and coincide with the northern flank of the South Shetland Trench at the base of the Antarctic continental slope (Fig. 1, 5, 7b).

Differences in location of the mean SAF and PF frontal jets and the O95 mean fronts may be due to differences in the spatial resolution of the ADCP dataset and the historical hydrography available to O95 (Section 3a, Fig. 5). Note that the disparity is starkest in the SAF where our sampling is densest and the Drake Passage historical hydrography is most sparse. Mean SAF front locations inferred by Gille (1994) by fitting Gaussian

jets to along-track gradients of altimetric sea level are displaced even further to the south than the O95 SAF and do not curve with the topography. This is not surprising for two reasons: firstly, the Geosat satellite data used by Gille (1994) had an inadequate tide model resulting in routine exclusion of the data in shallow water; secondly, the SAF may not meander enough in Drake Passage to be detected by Gille's (1994) jet-fitting algorithm. In the middle of Drake Passage, where the historical hydrography is less sparse and the altimetry is more accurate, we find the core of the observed mean PF jet to be bounded by the O95 PF 50 km to the south and the Gille (1994) PF 50 km to the north.

b. Variability

Variability in the surface-layer velocities is quantified by estimating EKE and eddy momentum fluxes from the ADCP observations. Significant surface intensification between the upper- and lower-layer EKE estimates from the LMG observations is greatest in the SAF and present everywhere in Drake Passage except for the region between the SAF and PF (Table 1). Observed velocity differences across the base of the mixed layer $\left(\frac{1}{2}|\Delta\vec{U}_{ml}|^2\right)$ indicate that inertial currents can fully account for the differences between the observed upper- and lower-surface layer EKE (Table 1, Section 4b) although this is true only at the limit of the standard errors in the SAF region. Shear in the baroclinic tides on the Patagonian continental slope may also contribute to the surface-intensification of EKE in the SAF. Thus the surface-intensification of the mixed-layer EKE can be attributed to ageostrophic processes. However it is interesting to note the lower-surface-layer EKE estimates, where the inertial currents are expected to be small, are much higher than those from moored observations of subsurface currents in Drake Passage (Table 3, Sciremammano *et al.*, 1980). These differences are consistent with a tendency for surface intensification of EKE observed in the ACC (Nowlin *et al.*, 1985; Bryden and Heath, 1985; Phillips and Rintoul, 2002).

The merged-altimeter AVISO sea-level anomalies produce higher EKE estimates between the SAF and PF in Drake Passage as compared with Stammer (1998) and Morrow *et al.* (1994) (Fig. 9 and Table 3). However, the AVISO-based EKE is still significantly lower than the ADCP EKE (Section 44, 9), accounting for 46–68% of the ADCP EKE in northern Drake Passage and 17% of the ADCP EKE south of the PF (Table 3). Some of the discrepancy between the AVISO and ADCP EKE can be explained by the spatial-smoothing inherent in the merged-satellite AVISO product at all wavelengths (Section 4a), a deficiency most pronounced at short wavelengths.

Inertial waves and baroclinic tides are expected to propagate at wavelengths <100 km. Our results show that inertial currents cause surface-intensification of EKE in the top 300 m, but they can only account for at most 10–22% of the total depth-averaged surface-layer EKE in northern Drake Passage and 49% south of the PF (Section 4b and Table 1). The ISOS/FDRAKE moored observations indicate that kinetic energy in the baroclinic tides

Table 3. Eddy momentum flux estimates ($cm^2\ s^{-2}$) from different observations of the ACC in the Southern Ocean.

Reference	Location	EKE ($cm^2 s^{-2}$)	Mean
		Current meters	
Scriremammano *et al.* (1980)	PF in DP (282 m)	205	Record length (10 months)
	(586 m)	128	
	(2010m)	23	
	(3521 m)	33	
Bryden and Heath (1985)	south of NZ[2] (1000 m)	169	Record length (2 years)
Phillips and Rintoul (2000)	SAF, 143°E, (420 db)	339	Geographic coord. (2 years)
		136	SC[3]
		ALACE Floats	
Gille (2003b)	Southern Ocean (900 m)	147 ± 34	Eulerian mean [4] (10+ years)
		Altimetry	
Morrow *et al.* (2003)	SAF, 150°E	O(200) (standing)	3-year Eulerian mean,
		O(450) (transient)	(9-year record)[5]
Morrow *et al.* (1994)	northern DP	O(250)	Eulerian mean (2 years)
Stammer (1998)	northern DP	O(300)	Eulerian mean (3+ years)
This study	SAF in DP	270	3-year Eulerian mean,
	DP, between fronts	420	(10-year record)
	PF in DP	250	
	south of PF, DP	29	
		ADCP (30–300 m)	
This study	SAF in DP	591 ± 25	Eulerian mean,
	DP, between fronts	785 ± 57	(5+ years)
	PF in DP	369 ± 19	
	south of PF, DP	174 ± 7	

[1]DP = Drake Passage; [2]NZ = New Zealand; [3]SC = time-dependent stream co-ordinates;
[4] referenced to merged float and atlas mean, estimates averaged along streamlines;
[5] record length is shown where this exceeds period used to compute mean.

is small and may account for at most an additional 2–4% of the EKE in the surface-layer currents in central Drake Passage and 9% south of the mean PF (Section 4c). Baroclinic tidal kinetic energy is most likely higher close to the continental shelves; barotropic tides on the Patagonian shelf are strong (10–70 cm s^{-1} amplitude), as determined from the ADCP velocities (not shown) and TPXO6.2 predictions.

Surface-layer transport anomalies have a standard deviation of 3 Sv and contain high-frequency variability; for example a 7 Sv increase in track M transport occurs in just over a week in September 2001 (Fig. 8). Transport variability of the upper 125-m

layer, where inertial motions are largest, is only slightly larger than in the 125-m to 250-m layer. This suggests that inertial motions roughly cancel in the transport integral. We estimate less than 1 Sv of the surface-layer transport variability is due to inertial motions. Barotropic variability may also contribute to the transport variability. Recent studies by Weijer and Gille (2005) and Hughes *et al.* (2003, 1999) provide evidence that the high frequency fluctuations (>1 cycle yr^{-1}) in ACC transport are primarily due to the barotropic response of the ocean to wind. Fluctuations in net ACC transport above 2500 m on timescales of a month or less correspond to 2 Sv of variability in the top 250 m (Whitworth and Peterson, 1985). The combined inertial and barotropic variability is thus $\sqrt{5}$ Sv which accounts for most of the 3 Sv standard deviation in the transport estimates.

c. Relationship between the mean flow and eddy fluxes

We observe the down-passage velocity anomaly spectrum to be peaked, with more variance at wavenumbers above the peak than below (solid black line in Fig. 10b). The peak wavelength (250 km, Fig. 10b) is about twice the mean width of the frontal jets ($\sim$110 km, Fig. 4b). The spectrum and the jet-width scale suggest possible application of geostrophic turbulence theory. Rhines (1975) examined freely-decaying turbulence on a barotropic β-plane and found that the turbulent energy of mesoscale eddies accumulates in the zonal velocity component and cascades to ever-larger scales up to a maximum wavenumber ($k_\beta = \sqrt{\frac{\beta}{U}}$ where U is the rms velocity and β is the meridional gradient of planetary vorticity). Consequently, the wavenumber spectrum is expected to peak at k_β and to drop abruptly at smaller wavenumbers; at long time scales the flow organizes into zonal jets. Vallis and Maltrud (1993) show that the zonal jet widths scale with πk_β^{-1}, half the peak wavelength. In baroclinic flow with topography, there is no exact analogy with the β-effect in Rhines's (1975) theory. Our estimate of the Rhines scale $\left(2\pi k_\beta^{-1}\right)$ in Drake Passage is $\sim$1100 km, where $U \sim 40$ cm s^{-1} and $\beta \sim 1.2 \times 10^{-11}$ m^{-1} s^{-1}. This exceeds the width of Drake Passage and is much larger than the peak wavelength of the velocity anomaly spectra (Fig. 10b). Lateral boundaries and topography, however, reduce jet widths and spacing in idealized models; Sinha and Richards (1999) find some support for a modified Rhines scaling in the Fine Resolution Antarctic Model, but their analysis of the Parallel Ocean Program model indicates that additional factors are probably important. The dominance of the cross-passage spectrum (dashed black line in Fig. 10b) at wavelengths longer than 250 km is not predicted by geostrophic turbulence arguments and suggests some other process must also be contributing to the spectral peaks. The relevance of a modified Rhines scaling to the wavenumber spectral characteristics we have observed in Drake Passage remains an open question.

The zonal momentum input to the Southern Ocean by the wind is thought to be balanced by the meridional divergence of depth-integrated $\langle\overline{u'v'}\rangle$ and eddy-form drag that results from a poleward eddy heat flux $\langle\overline{v'T'}\rangle$, where T is temperature (Johnson and Bryden, 1989). Gill

(1968) calculated that for the meridional divergence of $\langle\overline{u'v'}\rangle$ to directly balance the wind stress input to the circumpolarly-unbounded latitudes of the Southern Ocean (56.5°S to 61.5°S), $\langle\overline{u'v'}\rangle$ of O(100 cm^2 s^{-2}) is required on the edges of this latitude band. However, prior observations have shown $\langle\overline{u'v'}\rangle$ to be much smaller than 100 cm^2 s^{-2} or insignificant in the Southern Ocean (Bryden, 1979; Bryden and Heath, 1985; Morrow *et al.*, 1994; Phillips and Rintoul, 2000). Our results show that in the surface layer between the SAF and PF, $\langle\overline{u'v'}\rangle$ is significantly negative and of the order of magnitude predicted by Gill (1968); $\langle\overline{u'v'}\rangle$ is zero elsewhere in Drake Passage. Although we are presently unable to resolve the eddy forcing of the down-passage mean flow $\frac{\partial\langle\overline{u'v'}\rangle}{\partial y}$, Table 3 indicates that there is a tendency for $\frac{\partial\langle\overline{u'v'}\rangle}{\partial y}$ to be positive on the south flank of the mean SAF and negative farther south in Drake Passage. The orientation of the standard deviation ellipses also depends on $\langle\overline{u'v'}\rangle$; major axes of the finely-gridded standard deviation ellipses appear to turn from the fourth to the first quadrant equatorward along tracks W and E (i.e. turning from approximately east to northeast in geographic co-ordinates), corresponding to positive $\frac{\partial\langle\overline{u'v'}\rangle}{\partial y}$ south of the mean SAF (Fig. 6b). However, the pattern does not hold along track M where the ellipses appear to be aligned with the mean current (except at $y_{pc} = -150$ km), contributing to the large errors in $\langle\overline{u'v'}\rangle$. Taken together, the horizontal-wavenumber spectra and our $\langle\overline{u'v'}\rangle$ estimates suggest that transient eddies affect the dynamics of the ACC fronts in Drake Passage. There has been some effort to determine whether these eddies act to accelerate or decelerate the frontal jets (Morrow *et al.*, 1994; Hughes and Ash, 2001), but the question remains open.

A comparison of EKE estimates elsewhere in the Southern Ocean places our Drake Passage results in context and highlights the variation of Southern Ocean mesoscale variability. EKE estimates from deep moorings (Sciremammano *et al.*, 1980; Bryden and Heath, 1985; Phillips and Rintoul, 2000) are generally lower than the corresponding altimetric estimates (Morrow *et al.*, 1994, 2003; Stammer, 1998), vary zonally and are sensitive to calculation technique (Table 3). In particular, techniques that attempt to distinguish transient eddies from the meandering ACC fronts give different results from calculations of EKE and eddy fluxes relative to a time mean (Nowlin *et al.*, 1985; Phillips and Rintoul, 2002; Morrow *et al.*, 2003). This distinction is important because it is the transient eddies, and not the meandering ACC fronts, that are thought to transfer heat and momentum in the Southern Ocean. However, former strategies such as averaging fluxes along time-dependent streamlines inferred from vertical current shear (Phillips and Rintoul, 2002) or two-dimensional fields of temperature and pressure (Meinen and Luther, 2003), or by separating meanders from transient eddies in frequency space (Nowlin *et al.*, 1985; Morrow *et al.*, 2003) cannot be applied to the LMG ADCP data set.

6. Conclusions

The mean ACC through Drake Passage has been previously characterized by the FDRAKE/ISOS moorings and the SR1 summer shipboard hydrographic observations. The

LMG ADCP observations complement these studies by providing the first highly-resolved, frequent-repeat observations of velocity in the surface layer of Drake Passage. Crucially, these new observations span the mixed layer, where there are few moored observations, and occur frequently throughout the year.

Our ADCP observations resolve the convergence of multiple filaments of the PF and SACCF into two well-defined mean frontal jets as the ACC flows through Drake Passage. Finely-gridded mean currents resolve the standing meander in the SAF (Fig. 6a), showing that the SAF first turns northward as it enters Drake Passage and then eastward to follow the bathymetric contours of the Patagonian continental slope more closely than climatology suggests (O95). The mean surface-layer transport is 27.8 ± 1 Sv, about 20% of the total ACC transport estimated from SR1 (Cunningham *et al.*, 2003).

Estimates of eddy momentum fluxes and EKE from the ADCP observations quantify the surface-layer mesoscale variability in Drake Passage. EKE estimates are $\geq 200\,\mathrm{cm}^2\,\mathrm{s}^{-2}$ across Drake Passage and rise significantly to $785\,\mathrm{cm}^2\,\mathrm{s}^{-2}$ in the region between the SAF and PF. Surface intensification of the mixed-layer EKE can be attributed primarily to near-inertial oscillations. Horizontal-wavenumber spectra indicate that mesoscale variability with wavelengths >100 km constitutes 84% of the ADCP velocity variance in Drake Passage. At these wavelengths, mesoscale activity resolved by the AVISO satellites accounts for $\sim$50% of the ADCP variance. Region-by-region comparisons show that the altimetry resolves 46–68% of the total ADCP EKE estimates in northern Drake Passage. In the same region, inertial currents and baroclinic tides that propagate at length scales <100 km account for at most 14–31% of the ADCP estimate. South of the mean PF, inertial and tidal variability accounts for at most 66% of total ADCP EKE while the altimetry accounts for only 17%. This leads us to conclude that the mesoscale eddies and meanders are chiefly responsible for the variability in the two northern ACC fronts and the region between, while inertial currents are more important south of the mean PF in Drake Passage. Discrepancies between the Drake Passage ADCP EKE estimates and the combined altimetric, inertial and baroclinic tidal EKE are significant at 95% confidence north of the PF. The discrepancies are principally due to underestimates of mesoscale variability at all wavelengths in the AVISO altimetry.

The character of the down-passage velocity spectra and the variation in $\langle\overline{u'v'}\rangle$ with latitude (Section 3a, 4 and 4a) imply that eddy-mean flow interaction occurs in Drake Passage. Better statistics are required to compute the divergence of the $\langle\overline{u'v'}\rangle$ momentum flux and resolve the nature of the eddy-mean flow interaction. The meridional heat flux is also of interest; however, this quantity cannot yet be resolved from the observations presently available. Our statistics would be improved if data from all the LMG transects can be combined by projecting the ADCP velocities along mean streamlines. Defining these mean streamlines and developing a method to estimate time-dependent streamlines remain topics of on-going work. Continued observations of currents and upper ocean temperature at high spatial and temporal resolution are also essential for improving our statistics and our understanding of the dynamics of the ACC and the upper ocean in Drake Passage.

Acknowledgments. We acknowledge the National Science Foundation (NSF) Office of Polar Programs (OPP) and Division of Ocean Sciences (OCE) for sponsoring the ADCP and XBT observing programs on the LMG and this research through grants OPP-9816226/0338103, OCE-0327544, OPP-0337998, and OPP-9816483/0337375. ECMWF ERA-40 data used in this study have been obtained from the ECMWF data server (http://data.ecmwf.int/data/d/era40_daily/). The altimeter product used in these analyses was produced by SSALTO/DUACS and distributed by AVISO with support from CNES. We are grateful to the captain and crew of the RVIB *Laurence M. Gould* and to Raytheon Polar Services Corporation for their excellent technical and logistical support on the cruises. We thank Jules Hummon for her invaluable contribution to the ADCP data collection and processing on the LMG and the RVIB *Nathaniel B. Palmer*. We also thank Sarah Gille for her advice on wind products, Luc Rainville, Jen Mackinnon and Jody Klymak for their internal wave expertise and Sharon Escher who has been instrumental in the processing and editing of the LMG ADCP data.

REFERENCES

Alford, M. H. 2003. Improved global maps and 54-year history of wind-work on ocean inertial motions. Geophys. Res. Lett., *30*, 1424, doi:10.1029/2002GLO16614.

Alford, M. H. and M. Whitmont. 2007. Seasonal and spatial variability of near-inertial kinetic energy from historical moored velocity records. J. Phys. Oceanogr., (in press).

Belkin, I. M. and A. L. Gordon. 1996. South Ocean fronts from the Greenwich Meridian to Tasmania. J. Geophys. Res., *101*, 3675–3696.

Botnikov, V. N. 1963. Geographical position of the Antarctic Convergence Zone in the Southern Ocean, *in* Information of the Soviet Antarctic Expedition (Eng. Trans), Volume 4, 324–327.

Bromwich, D. H. and R. L. Fogt. 2004. Strong trends in the skill of the ERA-40 and NCEP-NCAR reanalysis in the high and midlatitudes of the Southern Hemisphere, 1958–2001. J. Climate, *17*, 4603–4619.

Bryden, H. L. 1979. Poleward heat flux and conversion of available potential energy in Drake Passage. J. Mar. Res., *37*, 1–22.

Bryden, H. L. and R. Heath. 1985. Energetic eddies at the northern edge of the Antarctic Circumpolar Current in the southwest Pacific. Prog. Oceanogr., *14*, 65–87.

Chereskin, T., E. Firing and J. Hummon. 2000. High resolution ADCP measurements across Drake Passage. EOS Trans., *83*.

Chereskin, T. and A. J. Harding. 1993. Modeling the performance of an Acoustic Doppler Current Profiler. J. Atmos. Oceanic Technol., *10*, 43–63.

Chereskin, T. K. and C. L. Harris. 1997. Shipboard acoustic doppler current profiling during the WOCE Indian Ocean expediton: I10., Technical Report SIO 97-14, Scripps Institution of Oceanography.

Cunningham, S. A., S. G. Alderson, B. A. King and M. A. Brandon. 2003. Transport and variability of the Antarctic Circumpolar Current in Drake Passage. J. Geophys. Res., *108*, doi:10.1029/2001JC001147.

Dong, S. F., S. T. Gille and J. Sprintall. 2006. Validation of the Advanced Microwave Scanning Radiometer for the Earth Observing System (AMSR-E) sea surface temperature in the Southern Ocean. J. Geophys. Res., *111*, doi:10.1029/2005JC002834.

Ducet, N., P. Y. Le Traon and G. Reverdin. 2000. Global high-resolution mapping of ocean circulation from TOPEX/Poseidon and ERS-1 and -2. J. Geophys. Res., *105*, 19,477–19,498.

Egbert, G. D., A. F. Bennett and M. Foreman. 1994. TOPEX/Poseidon tides estimates using a global inverse model. J. Geophys. Res., *99*, 24821–24852.

Emery, W. J. 1977. Antarctic Polar Frontal Zone from Australia to Drake Passage. J. Phys. Oceanogr., *7*, 811–822.

Gill, A. E. 1968. A linear model of the Antarctic Circumpolar Current. J. Fluid Mech., *32*, 465–488.

Gille, S. T. 1994. Mean sea surface height of the Antarctic Circumpolar Current from Geosat data: Method and application. J. Geophys. Res., *99*, 18255–18273.

—— 2003a. Float observations of the Southern Ocean. Part I: Estimating mean fields, bottom velocities, and topographic steering. J. Phys. Oceanogr., *33*, 1167–1182.

—— 2003b. Float observations of the Southern Ocean. Part II: Eddy fluxes. J. Phys. Oceanogr., *33*, 1182–1196.

Gouretski, V. V. and K. Jancke. 1998. A new climatology for the world ocean, *in* WHP SAC Tech. Rep. No. 3, WOCE Report No. 162/98, WOCE Special Analysis Centre, Max Planck Institute, Hamburg.

Holliday, N. and J. Read. 1998. Surface oceanic fronts between Africa and Antarctica. Deep-Sea Res. I, *45*, 217–238.

Hughes, C. W. and E. R. Ash. 2001. Eddy forcing of the mean flow in the Southern Ocean. J. Geophys. Res., *106*, 2713–2722.

Hughes, C. W., M. P. Meredith and K. Heywood. 1999. Wind-driven transport fluctuations through Drake Passage: A Southern Mode. J. Phys. Oceanogr., *29*, 1971–1992.

Hughes, C. W., P. L. Woodworth, M. P. Meredith, V. Stepanov, T. Whitworth, III. and A. R. Pyne. 2003. Coherent Antarctic sea levels, Southern Hemisphere annular mode, and flow through Drake Passage. Geophys. Res. Lett., *30*, doi:10.1029/2003GL017240.

Johnson, G. C. and H. L. Bryden. 1989. On the size of the Antarctic Circumpolar Current. Deep-Sea Res., *36*, 39–53.

Joyce, T. M., W. Zenk and J. Toole. 1978. The anatomy of the Antarctic Polar Front in Drake Passage. J. Geophys. Res., *83*, 6093–6114.

King, B. A. and E. B. Cooper. 1993. Comparison of ship's heading determined from an array of GPS antennas with heading from conventional gyrocompass measurements. Deep-Sea Res. I, *40*, 2207–2216.

Large, W. G. and S. Pond. 1981. Open ocean momentum flux measurements in moderate and strong winds. J. Phys. Oceanogr., *11*, 324–336.

Le Traon, P. Y., F. Nadal and N. Ducet. 1997. An improved mapping method of multi-satellite altimeter data. J. Atmos. Ocean. Tech., *15*, 522–534.

Levitus, S. and T. Boyer. 1994. World Ocean Atlas 1994, NOAA Atlaas NESDIS 4, U.S. Department of Commerce, Washington, D.C.

Maltrud, M. E., R. Smith, A. J. Semtner and R. C. Malone. 1998. Global eddy-resolving ocean simulations driven by 1985-1995 atmospheric winds. J. Geophys. Res., *103*, 825–30.

Meinen, C. S. and D. S. Luther. 2003. Comparison of methods of estimating mean synoptic current structure in"stream coordinates" reference frames with an example from the Antarctic Circumpolar Current. Deep-Sea Res. I, *50*, 201–220.

Moore, J. K., M. R. Abbott and J. G. Richman. 1999. Location and dynamics of the Antarctic Polar Front from satellite sea surface temperature data. J. Geophys. Res., *104*, 3059–3073.

Morrow, R., A. Brut and A. Chaigneau. 2003. Seasonal and interannual variations of the upper ocean energetics between Tasmania and Antarctica. Deep-Sea Res. I, *50*, 339–356.

Morrow, R., R. Coleman, J. Church and D. Chelton. 1994. Surface eddy momentum flux and velocity variances in the Southern Ocean from Geosat altimetry. J. Phys. Oceanogr., *24*, 2050–2071.

Niiler, P. P., N. A. Maximenko and J. C. McWilliams. 2003. Dynamically balanced absolute sea level of the global ocean derived from near-surface velocity observations. Geophys. Res. Lett., *30*, doi:10.1029/2003GL018628.

Nowlin, Jr., W., T. Whitworth, III. and R. Pillsbury. 1977. Structure and transport of the Antarctic Circumpolar Current at Drake Passage from short-term measurements. J. Phys. Oceanogr., *7*, 788–802.

Nowlin, Jr., W., S. J. Worley and T. Whitworth, III. 1985. Methods for making point estimates of eddy heat flux as applied to the Antarctic Circumpolar Current. J. Geophys. Res., *90*, 3305–3324.

Olbers, D., V. Gouretski, G. Seiß and J. Schröter. 1992. Hydrographic atlas of the Southern Ocean, Technical report, Alfred Wegener Institut, Bremerhavan, 17 pp. and 82 plates.

Orsi, A. H., T. Whitworth, III. and W. D. Nowlin, Jr. 1995. On the meridional extent and fronts of the Antarctic Circumpolar Current. Deep-Sea Res. I, *42*, 641–673.

Padman, L., S. Howard and R. Muench. 2006. Internal tide generation along the South Scotia Ridge. Deep-Sea Res. II, *53*, 157–171.

Phillips, H. E. and S. Rintoul. 2000. Eddy variability and energetics from direct current measurements in the Antarctic Circumpolar Current south of Australia. J. Phys. Oceanogr., *30*, 3050–3076.

—— 2002. A mean synoptic view of the Subantarctic Front South of Australia. J. Phys. Oceanogr., *32*, 1536–1553.

Pillsbury, R., T. Whitworth, III., W. D. Nowlin, Jr. and F. Sciremammano, Jr. 1979. Currents and temperatures as observed in Drake Passage. J. Phys. Oceanogr., *9*, 469–482.

Pollard, R. T. and R. Millard, Jr. 1970. Comparison between observed and simulated wind-generated inertial oscillations. Deep-Sea Res., *17*, 813–821.

Rhines, P. B. 1975. Waves and turbulence on a beta-plane. J. Fluid Mech., *69*, 417–443.

Sciremammano, Jr., F., R. Pillsbury, W. D. Nowlin, Jr. and T. Whitworth, III. 1980. Spatial scales of temperature and flow in Drake Passage. J. Geophys. Res., *85*, 4015–4028.

Simmons, H. L., R. W. Hallberg and B. Arbic. 2004. Internal wave generation in a global baroclinic tide model. Deep-Sea Res. II, *51*, 3043–3068.

Sinha, B. and K. J. Richards. 1999. Jet structure and scaling in Southern Ocean models. J. Phys. Oceanogr., *29*, 1143–1155.

Sokolov, S. and S. Rintoul. 2002. Structure of the Southern Ocean fronts at 140°E. J. Mar. Syst., *37*, 151–184.

Sparrow, M. D., K. Heywood, J. Brown and D. P. Stevens. 1996. Current structure of the south Indian Ocean. J. Geophys. Res., *103*, 6377–6391.

Sprintall, J. 2003. Seasonal to interannual upper-ocean variability in the Drake Passage. J. Mar. Res., *61*, 25–57.

Stammer, D. 1998. On eddy characteristics, eddy transports, and mean flow properties. J. Phys. Oceanogr., *28*, 727–739.

Uppala, S., P. Kållberg, A. Simmons, U. Andrae, V. da Costa Bechtold, M. Fiorino, J. Gibson, J. Haseler, A. Hernandez, G. Kelly, X. Li, K. Onogi, S. Saarinen, N. Sokka, R. Allan, E. Andersson, K. Arpe, M. Balmaseda, A. Beljaars, L. van de Berg, J. Bidlot, N. Bormann, S. Caires, F. Chevallier, A. Dethof, M. Dragosavac, M. Fisher, M. Fuentes, S. Hagemann, E. Hólm, B. Hoskins, L. Isaksen, P. Janssen, R. Jenne, A. McNally, J.-F. Mahfouf, J.-J. Morcrette, N. Rayner, R. Saunders, P. Simon, A. Sterl, K. Trenberth, A. Untch, D. Vasiljevic, P. Viterbo and J. Woollen. 2005. The ERA-40 re-analysis. Quart. J. R. Meteorol. Soc., *131*, 2961–3012.doi:10.1256/qj.04.176.

Vallis, G. K. and M. E. Maltrud. 1993. Generation of mean flows and jets on a beta plane and over topography. J. Phys. Oceanogr., *23*, 1346–1362.

Weijer, W. and S. T. Gille. 2005. Adjustment of the Southern Ocean to wind forcing on synoptic time scales. J. Phys. Oceanogr., *35*, 2076–2089.

Whitworth, III., T. 1980. Zonation and geostrophic flow of the Antarctic Circumpolar Current at Drake Passage. Deep-Sea Res. Part A, *27*, 497–507.

—— 1983. Monitoring the Transport of the Antarctic Circumpolar Current at Drake Passage. J. Phys. Oceanogr., *13*, 2045–2057.

Whitworth, III., T. and R. Peterson. 1985. Volume transport of the Antarctic Circumpolar Current from bottom pressure measurements. J. Phys. Oceanogr., *15*, 810–816.

Yelland, M. and P. K. Taylor. 1996. Wind stress measurements from the open ocean. J. Phys. Oceanogr., *26*, 541–558.

Received: *18 April, 2006*; revised: *1 December, 2006*.